AIAA JOURNAL
Vol. 59, No. 9, September 2021

Hypersonic Boundary-Layer Receptivity over a Blunt Cone to Freestream Pulse Disturbances

Simon He* and Xiaolin Zhong†
University of California, Los Angeles, California 90095

https://doi.org/10.2514/1.J059697

Although receptivity plays a key role in the transition of hypersonic flows, most prior computational receptivity studies have neglected to study broadband frequency disturbance spectra. This work uses perfect gas linear stability theory (LST) and direct numerical simulation (DNS) to study the receptivity of flow over a 9.525 mm nose radius, 7 deg half-angle straight cone at Mach 10 using finite spherical and planar pulses to approximate disturbances with broadband frequency spectra. Freestream fast acoustic, slow acoustic, temperature, and vorticity pulses of both geometries were studied to investigate a wide range of forcing conditions. Unsteady DNS predicts second mode growth and agrees well with LST. DNS and LST data are used to extract second mode receptivity coefficients and phase spectra. For the finite pulses the strongest to weakest responses are for the fast acoustic, temperature, slow acoustic, and vorticity pulses, respectively. The planar disturbances show the strongest response for the slow acoustic, temperature, vorticity, and fast acoustic pulses in that order. Fast Fourier transform results show significant variation in the spectral disturbance response between disturbance types and geometries, and the planar fast acoustic pulse in particular is shown to much more readily excite modal disturbances other than the primary second mode.

Nomenclature

C_{rec}	=	receptivity coefficient
c_r	=	nondimensional phase speed
c_∞	=	disturbance velocity, m/s
f	=	frequency, Hz
L^*	=	boundary-layer thickness parameter, m
M	=	Mach number
Pr	=	Prandtl number
Re	=	Reynolds number
s^*	=	streamwise position, m
T	=	temperature, K
α	=	spatial wavenumber, 1/m
ϵ	=	peak freestream disturbance amplitude
σ	=	Gaussian shape parameter
ϕ	=	phase angle
ω	=	circular frequency

Subscripts

i	=	imaginary component
r	=	real component
w	=	wall
0	=	stagnation
∞	=	freestream

I. Introduction

THE accurate prediction of laminar to turbulent transition in hypersonic flows is a major concern when using computational fluid dynamics (CFD) to aid in the design of hypersonic vehicles. Transition to turbulence is known to dramatically increase aerodynamic drag and heating on the vehicle's surface and significantly affect the control of the vehicle [1–3]. Effectively delaying and/or predicting transition in hypersonic vehicles will allow for greater specificity in the design of thermal protection systems (TPSs) to minimize their weight impact and improve payload capacities.

Transition in a hypersonic boundary layer is governed by several mechanisms, and in the case of weak environmental forcing it can be broken down into three distinct stages: 1) boundary-layer receptivity, 2) linear growth of small amplitude disturbances, and 3) nonlinear breakdown at finite disturbance amplitudes [4]. Traditionally, studies on hypersonic boundary-layer transition at zero angle of attack have focused on the linear growth of Mack modes, for which the second mode instability has been found to dominate [5]. However, receptivity mechanisms dictate the initial disturbance amplitudes of flow instabilities like the second mode, and can greatly impact the general stability behavior of the flow [6]. Studies of receptivity commonly focus on the response to freestream noise which, for compressible flows, can be categorized into three distinct types: acoustic, entropy, and vorticity disturbances [7]. In hypersonic flows the interaction of any of these freestream disturbances with the bow shock generates disturbance waves of all three types behind the shock [8]. These can then propagate to and perturb the boundary layer. The mechanisms of the shock–disturbance interactions for each of these freestream disturbance types can vary significantly and cause differences in the resulting boundary-layer perturbations, in terms of both disturbance amplitude and phase [9]. Thus, a wide-ranging consideration of all the disturbance types is needed to fully characterize the receptivity of a hypersonic flow.

The receptivity of hypersonic boundary layers to freestream disturbances has been extensively studied in flows over flat plates [4,10–15] and cones [16–21]. Freestream acoustic, vorticity, and entropy disturbances modeled as discrete frequency planar waves were found to excite continuous and discrete mode instabilities to varying degrees in flat plates [4,10,14]. Acoustic disturbances in particular were seen to most readily excite the unstable second mode in flat plates [4,13], though the other disturbance types were also shown to potentially generate weaker modal instabilities [14]. Acoustic disturbances were also found to excite the strongest second mode response in cone geometries [16,18], though entropy and vorticity disturbances were able to excite second mode instabilities much more readily than in the flat plate cases. The additional complexity introduced by the bow shock and surface curvature for cones were observed to present different receptivity paths for freestream disturbances and necessitates studying a wide variety of disturbances to fully characterize the receptivity response of hypersonic flow over a cone.

Presented as Paper 2020-2996 at the AIAA Aviation 2020 Forum, Virtual Event, June 15–19, 2020; received 26 May 2020; revision received 1 February 2021; accepted for publication 16 March 2021; published online 25 June 2021.

*Ph.D. Student, Mechanical and Aerospace Engineering Department; simon.he.ucla@gmail.com. Student Member AIAA.

†Professor, Mechanical and Aerospace Engineering Department; xiaolin@seas.ucla.edu. Associate Fellow AIAA.

Many of these prior receptivity studies simulated the boundary-layer response to discrete frequency planar Fourier modes in the freestream, which generally results in all of the energy of the disturbance spectrum being assigned to the most unstable frequency. This can lead to overestimations of the resulting boundary-layer disturbance amplitudes [19]. A more physically correct model would take into account a broadband distribution of excited disturbance frequencies. Several recent computational studies have investigated the response to more complex broadband disturbances. Balakumar and Chou [19] approximated broadband frequency spectra by simultaneously imposing carefully chosen combinations of discrete Fourier modes. They found that doing so allowed them to accurately predict transition on a sharp cone using a threshold criterion, though the accuracy decreased for their blunter cases. Huang and Zhong [9,22] instead used freestream Gaussian pulses in order to simulate laser spot experiments originally performed at Purdue by Wheaton et al. [23] and Chou et al. [24,25]. These preliminary works showed that pulses could also replicate broadband frequency freestream disturbances, that pulses and other broadband perturbations could excite significant modal instabilities, and that a consideration of broadband disturbances could improve the accuracy of predictions made using linear receptivity results. While the pulse model does not fully represent the stochastic nature of realistic flight disturbances, they provide more complex forcing environments than previously studied discrete planar waves and can be decomposed spectrally using fast Fourier transform (FFT) to generate databases of linear receptivity coefficients for different spatial forcing configurations. These receptivity data can be used to provide the initial disturbance amplitudes that are required by amplitude method-based transition estimation schemes.

The current study expands upon the work by Huang and Zhong and presents a novel consideration of additional disturbance types. Although the receptivity to different freestream disturbances has been extensively studied in the past, prior works have traditionally considered only discrete frequency disturbances or were limited in their selection of broadband disturbances. Though these works provide insight into the complex receptivity mechanisms present in hypersonic flows over cones, a more complete overview of the disturbance responses is necessary to further characterize the receptivity mechanisms present in hypersonic boundary layers. The receptivity mechanisms for both finite, spherical, and planar pulse geometries are investigated in this study. The different disturbance geometries result in different forcing interactions; the finite, spherical pulses are small relative to the nose radius of the cone and only interact with the domain in the nose region, whereas the planar pulse can continuously interact with the shock as it propagates in the streamwise direction. This study aims to investigate the effects of these two different disturbance regimes. Fast acoustic, slow acoustic, temperature, and vorticity disturbances are modeled using both of the pulse geometries for a total of eight unsteady cases. The mean flow geometry is based on experiments by Marineau et al. [26] for a Mach 10 flow over a cone from the AEDC wind tunnel 9. The numerical study in this paper consists of three primary components: 1) the steady mean flow simulation and linear stability theory (LST) analysis, 2) the unsteady direct numerical simulation (DNS) simulation using the freestream pulse disturbances, and 3) the generation of the spectral receptivity coefficients and phase angles using the LST and unsteady DNS results. Assuming a linear receptivity process, the resulting receptivity coefficients can be directly applied to the development of more advanced transition estimation procedures such as Mack's amplitude method [27,28] or Crouch's variable N-factor method [29]. Contrary to the conventional e^N method, these newer procedures are directly concerned with disturbance amplitudes themselves and not just the amplification ratio. Thus, they require receptivity data to directly estimate the initial disturbance amplitudes. Receptivity spectra, like the ones from this study, are necessary in order to generate more precise receptivity correlations. These can in turn be used to produce more precise estimates of initial disturbance amplitudes compared with commonly used empirically fitted data, and further improve the accuracy of these alternative transition prediction methods.

II. Simulation Conditions

The current study focuses on the receptivity of a 9.525 mm nose radius circular, straight cone with a half-angle of 7 deg at Mach 10 to freestream finite spherical fast acoustic, slow acoustic, temperature, and vorticity disturbances as well as freestream planar fast acoustic, slow acoustic, temperature, and vorticity disturbances. The perturbations were modeled as Gaussian pulses in the freestream, providing for broadband frequency disturbances. The cone geometry is 1.9 m in length along the line of symmetry. The DNS simulations used 240 points in the wall-normal direction and roughly five points per millimeter on the surface of the cone in the streamwise direction. Four points are used in the periodic spanwise direction, though only one point is directly calculated at each time step. The flow conditions for this study are summarized in Table 1 and are based on the tunnel conditions reported by Marineau et al. [26] for run 3752.

The DNS code used in this study uses a shock-fitting formulation with the parameters in Table 1 defining the freestream conditions upstream of the shock formed over the body. The viscosity used here was calculated using Sutherland's law, whereas Marineau et al. [26] instead used curve fits of experimental data. This leads to approximately a 15% increase in the calculated freestream unit Reynolds number in this study compared with Marineau's.

III. Numerical Methods and Disturbance Model

A. Direct Numerical Simulation

The DNS code uses a high-order shock-fitting method formulated for a perfect gas that computes the flowfield between the shock and the body. The numerical method is summarized here for clarity. The receptivity simulations in this study assume calorically perfect gas behavior for molecular nitrogen in the flowfield. This assumption was made based on the low freestream stagnation enthalpy reported in Table 1. The three-dimensional conservative Navier–Stokes system consists of a single species mass conservation equation, three momentum conservation equations, and the energy equation. The governing equations in vector form are written as

$$\frac{\partial U}{\partial t} + \frac{\partial F_j}{\partial x_j} + \frac{\partial G_j}{\partial x_j} = 0, \qquad (j = 1, 2, 3) \tag{1}$$

where U is the state vector of conserved quantities and F_j and G_j are the inviscid and viscous flux vectors, respectively. Here, the j indices indicate curvilinear coordinates in the streamwise, radial, and azimuthal directions about the cone. The conservative vector U comprises five conservative flow variables for mass, momentum, and energy. In the shock fitting code, both the shock itself and the surface of the cone are treated as computational boundaries for the grid. The physical domain is defined by curvilinear grids matching the curvature of the cone geometry. A schematic of this is given in Fig. 1.

The equations are transformed into uniform Cartesian computational coordinates in order to apply the high-order finite difference methods used in the shock-fitting algorithm. The transformed governing equation is

Table 1 Freestream flow conditions for DNS simulations

Parameter	Value
M_∞	9.79
ρ_∞	0.0427 kg/m^3
T_∞	51.0 K
$T_w/T_{0,\infty}$	0.3
Re/m (1E6/m)	18.95
$h_{0,\infty}$	1.07 MJ/kg
p_∞	0.65 kPa
U_∞	1426 m/s
Pr	0.72
Angle of attack	0°

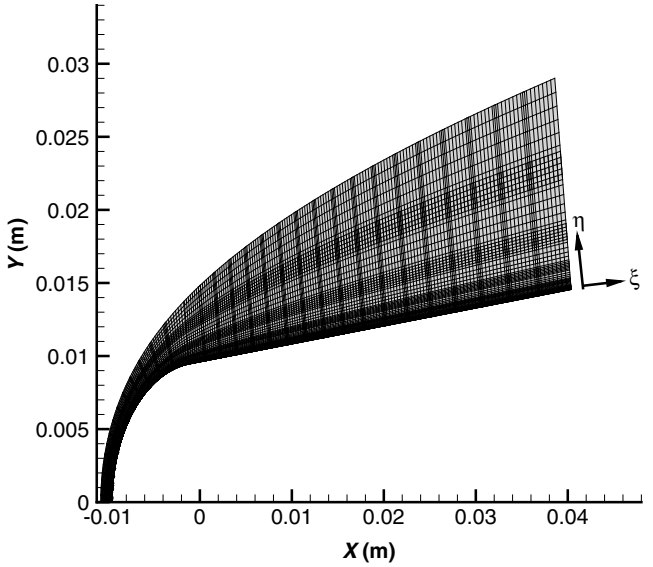

Fig. 1 Schematic of grids near nose region of cone. Grid density is coarsened for clarity.

$$\frac{1}{J}\frac{\partial U}{\partial \tau}+\frac{\partial E'}{\partial \xi}+\frac{\partial F'}{\partial \eta}+\frac{\partial G'}{\partial \zeta}+\frac{\partial E_{v'}}{\partial \xi}+\frac{\partial F_{v'}}{\partial \eta}+\frac{\partial G_{v'}}{\partial \zeta}+U\frac{\partial(1/J)}{\partial \tau}=0 \quad (2)$$

where J is the Jacobian of the coordinate transformation and (ξ, η, ζ) are the transformed computational coordinates in the streamwise, radial, and azimuthal directions of the cone. A low-dissipation, fifth-order upwinded stencil is used for the inviscid fluxes, whereas a sixth-order central stencil is used to discretize the viscous terms. The shock itself is treated as a computational boundary, the location of which is also solved for in the shock-fitting algorithm. The flow variables behind the shock are determined through a combination of the Rankine–Hugoniot relations across the shock and a characteristic compatibility relation behind the shock. Isothermal and viscous boundary conditions are imposed at the cone surface where the wall temperature ratio is fixed as $Tw/T_0 = 0.3$. High-order extrapolation is used at the domain outlet. Finally, the solution is advanced in time using a low-storage first-order Runge–Kutta method from Williamson [30]. The details of this shock-fitting formulation and the numerical methods can be found in Zhong [31].

B. Linear Stability Theory

The LST implementation used in this study was originally developed and verified by Ma and Zhong [4,11,12]. The LST relations are derived from the governing Navier–Stokes equations in Eq. (1), where the instantaneous flow is decomposed into a mean and fluctuating component $q = \bar{q} + q'$. This instantaneous flow is then reintroduced into the governing equations. Because the steady mean flow component is assumed to satisfy the governing equations, it can be subtracted out. The mean flow is also assumed to be quasi-parallel, and thus any remaining mean flow terms are functions of y only. Disturbances are also assumed to be small enough that quadratic and higher-order perturbation terms can be ignored, allowing for the linearization of the equations. A normal mode solution in the form of $q' = \hat{q}(y)\exp[i(\alpha x + \beta z - \omega t)]$ is introduced, where ω is the circular frequency of the disturbance, and α and β are the wavenumbers. In this study a spatial stability approach is used. Thus α is complex and results in the dispersion relation $\alpha = \Omega(\omega, \beta)$. For the spatial stability approach, the circular frequency of a disturbance mode, ω, must be manually set depending on the disturbance frequency of interest while β is set to 0 for a two-dimensional disturbance. The complex spatial wavenumber α is solved for and can be written as $\alpha = \alpha_r + i\alpha_i$. Here, $-\alpha_i$ is the growth rate of the disturbance. Substituting in the normal mode reduces the problem to a coupled set of five ordinary differential equations:

$$\left(\boldsymbol{A}\frac{d^2}{dy^2}+\boldsymbol{B}\frac{d}{dy}+\boldsymbol{C}\right)\vec{\phi}=\vec{0} \quad (3)$$

where $\vec{\phi} = [\hat{u}, \hat{v}, \hat{P}, \hat{T}, \hat{w}]^T$ and $\boldsymbol{A}$, $\boldsymbol{B}$, and $\boldsymbol{C}$ are complex square matrices of size five. This is now a boundary value problem where the derivative operators can be discretized and the equations solved numerically. The boundary conditions for Eq. (3) are given as

$$y = 0; \qquad \phi_1 = \phi_2 = \phi_3 = \phi_4 = \phi_5 = 0 \quad (4)$$

$$y \to \infty; \qquad \phi_1, \phi_2, \phi_3, \phi_4, \phi_5 \to 0 \quad (5)$$

The system of equations is solved using a multidomain spectral method similar to Malik [32]. The converged mean flow from the steady DNS is used as the input to the LST analysis where additional stretching for the multidomain spectral method is used to interpolate the mean flow results to the LST grids.

Although LST can be used to identify both the unstable disturbance frequencies and their growth rates, it does not directly specify the exact amplitude of the disturbance. Conventionally, boundary-layer transition is estimated using LST through an amplification criterion known as the e^N or the N-factor method. The N-factor is given by

$$e^{N(s^*,f)} = \frac{A(s^*,f)}{A_0(f)} = \exp\left[\int_{s_0^*}^{s^*} -\alpha_i(s^*,f)\mathrm{d}s^*\right] \quad (6)$$

Here $A(s^*, f)$ is spectral disturbance density at a position s^*, $A_0(f)$ is the initial disturbance density at the branch I neutral point s_0^*, and α_i is the spatial amplification rate (growth rate) obtained from LST. The growth rate is integrated for a discrete frequency in the streamwise direction using a trapezoidal method. Transition N-factors for sharp cones are commonly understood to be between 5 and 10. Lei and Zhong [33], Aleksandrova et al. [34], and Balakumar and Chou [19] found that N-factors decreased considerably at similar streamwise locations for blunter cones. Marineau et al. [26] also found that blunt nose N-factors calculated at the beginning of transition were significantly lower than those for sharp nose cases, reaching as low as 0.5. Pure considerations of the N-factor are observed to be insufficient to reliably determine transition throughout a wide variety of conditions.

C. Freestream Disturbance Model

The stability of the system is also studied by perturbing the mean flow and tracking the development of the boundary-layer disturbances using DNS. Here, the flow is disturbed with freestream fast acoustic, slow acoustic, temperature, and vorticity disturbances in the form of Gaussian pulses. Two pulse geometries, a finite spherical and a planar pulse distribution, were used in this work. Because the shock is treated as a computational boundary in the simulations, these pulses can be represented analytically in the freestream. A schematic of the unsteady simulation is given for the finite pulse case in Fig. 2a and for the planar pulse case in Fig. 2b. The finite spherical pulse is, as its name implies, a pulse disturbance that is limited spatially in x, y, and z. The pulse disturbance distribution is given in Eq. (7). The planar pulse is very similar and assumes that the dimensions of the pulse are fixed along the x axis. However, the disturbance remains infinite in the y and z directions. The pulses are advected by the freestream velocity along the central symmetry line of the cone. The limited scope of the finite spherical pulses causes them to only interact with cone near the nose region, whereas the planar pulses continue acting upon the flowfield throughout the entire domain as they propagate downstream. The design of the pulses is based on previous work by Huang and Zhong [9] and Lei and Zhong [21].

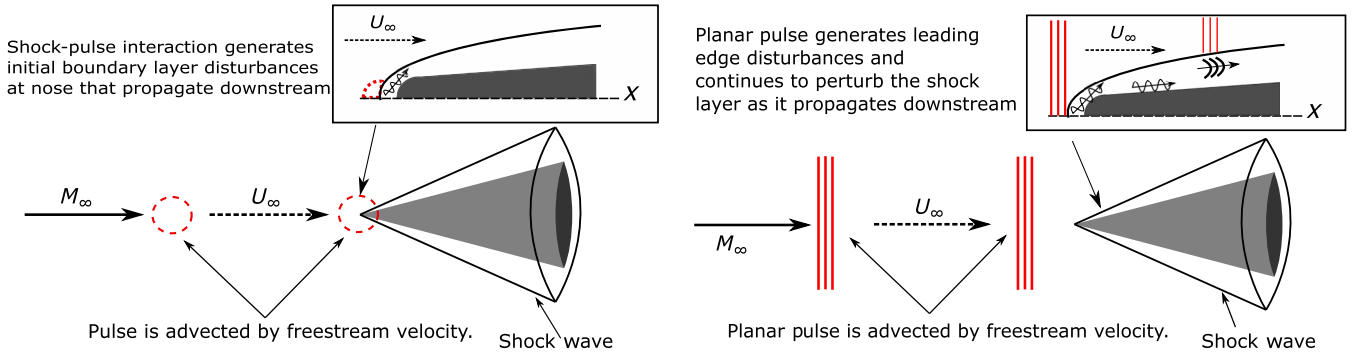

Fig. 2 Schematic diagram of unsteady simulation setup for a) a finite, spherical pulse disturbance, and b) a planar pulse disturbance in the freestream.

$$q(x, y, z, t) = |q'|_\infty \exp\left(-\frac{(R_c)^2}{2\sigma^2}\right) + q_\infty \tag{7}$$

The ϵM_∞ term governs the relative peak disturbance amplitude of the freestream pulse and was chosen to ensure that boundary-layer disturbances remained linear. Because the receptivity response to the planar pulses was expected to be much stronger than that for the finite spherical pulses, the amplitude parameter ϵM_∞ was reduced for these cases. This ϵM_∞ term is included in $|q'|_\infty$ in Eq. (7), which is further detailed in the dispersion relations in Eqs. (9–12) for the fast acoustic, slow acoustic, temperature, and vorticity disturbances, respectively. The term σ controls the width of the pulse and also determines the frequency content of the disturbance. This pulse width parameter was chosen to encompass significant freestream disturbances at frequencies up to 600 kHz in order to ensure the excitation of the primary modal instabilities predicted by LST and resulted in a pulse radius of approximately 3 mm. R_c refers to the radial distance from the center of the pulse to a point (x, y, z) in the flowfield. For a finite spherical pulse R_c is defined in Eq. (8).

$$R_c = \sqrt{(x - x_{\text{pulse}})^2 + (y - y_{\text{pulse}})^2 + (z - z_{\text{pulse}})^2} \tag{8}$$

Here, $(x_{\text{pulse}}, y_{\text{pulse}}, z_{\text{pulse}})$ denote the location of the pulse center. For the finite spherical pulses $y_{\text{pulse}} = z_{\text{pulse}} = 0$ is fixed. For the planar pulses, only the streamwise x-direction center point is taken into account and R_c reduces to $R_c = x - x_{\text{pulse}}$. For both geometries the pulse is advected in the streamwise direction by $x_{\text{pulse}} = x_0 + C_\infty t$, where C_∞ is the disturbance speed in the freestream. These speeds are defined as $C_\infty = U_\infty + a_\infty$ for fast acoustic disturbances, $C_\infty = U_\infty - a_\infty$ for slow acoustic disturbances, and $C_\infty = U_\infty$ for entropy/vorticity disturbances. Here U_∞ is the freestream velocity and a_∞ is the freestream speed of sound. To ensure that the same frequency spectrum is shared among the disturbances, the pulse width term σ must be scaled by $1 + 1/M_\infty$ for a fast acoustic disturbance and by $1 - 1/M_\infty$ for a slow acoustic disturbance.

The coefficient q corresponds to any perturbation variable in the freestream and q' is the peak perturbation amplitude of each of these variables normalized by the freestream value. In the case of a fast acoustic disturbance, the freestream disturbance amplitudes follow the dispersion relations given by [35]

$$|\rho'|_\infty = \frac{|P'|_\infty}{\gamma} = |u'|_\infty M_\infty = \epsilon M_\infty, \qquad |s'|_\infty = |v'|_\infty = 0 \tag{9}$$

A slow acoustic disturbance in the freestream is governed by a very similar dispersion relation:

$$|\rho'|_\infty = \frac{|P'|_\infty}{\gamma} = -|u'|_\infty M_\infty = \epsilon M_\infty, \quad |s'|_\infty = |v'|_\infty = 0 \tag{10}$$

A freestream entropy disturbance is described by

$$|\rho'|_\infty = -|s'|_\infty = \epsilon M_\infty, \qquad |u'|_\infty = |v'|_\infty = |p'|_\infty = 0 \tag{11}$$

And a freestream vorticity disturbance is described by

$$|v'|_\infty M_\infty = \epsilon M_\infty, \qquad |u'|_\infty = |p'|_\infty = |s'|_\infty = 0 \tag{12}$$

Because of the calorically perfect gas assumed in this study's numerical models, the temperature disturbances can be directly related to freestream entropy disturbances by the equation of state for a perfect gas.

The parameters given in Table 2 for the finite spherical cases result in the disturbance distribution shown in Fig. 3 and can be tuned accordingly to generate different spectral amplitude distributions. The frequency distribution of the planar disturbances follow the same trends as the finite spherical cases, with the only difference being a reduction in the peak freestream amplitude ϵM_∞ to ensure linear boundary-layer disturbances.

D. Boundary-Layer Receptivity

The boundary-layer disturbance content is studied by decomposing the surface pressure perturbations resulting from each pulse into their spectral frequency components using Fourier analysis. The time-dependent perturbation variables can be expressed in terms of their Fourier spectral components, obtained through an FFT:

$$h(t_k) \equiv h_k \approx \sum_{n=0}^{N-1} H(f_n) e^{-2\pi i f_n t_k} \tag{13}$$

where $H(f_n)$ is the frequency space Fourier coefficient corresponding to the nth discretized frequency f_n. Additionally, N corresponds to the total number of Fourier collocation points used to discretize the time-dependent function $h(t)$ in Fourier space. The discretized time function h_k is defined as being the value of the time-dependent function $h(t)$ at a given time $t = t_k$.

In this study, the variable $h(t_k)$ corresponds to local boundary-layer perturbations in the surface pressure. The complex components of $H(f_n)$ correspond to the phase angle of the perturbation variables through $\phi = \tan^{-1}(\text{Im}(H(f_n))/\text{Re}(H(f_n))$, and $|H(f_n)|$ are the perturbation amplitudes for the surface pressure at the frequency f_n.

Because LST was used to validate the results of the unsteady DNS analysis, local growth rates and wavenumbers need to be calculated from the Fourier decomposed perturbation data. Following a similar

Table 2 Gaussian pulse parameters for DNS

Pulse geometry	ϵM_∞	σ	x_0
Finite spherical	$5E-4$	$1E-3$	−0.02 m
Planar	$1E-6$	$1E-3$	−0.02 m

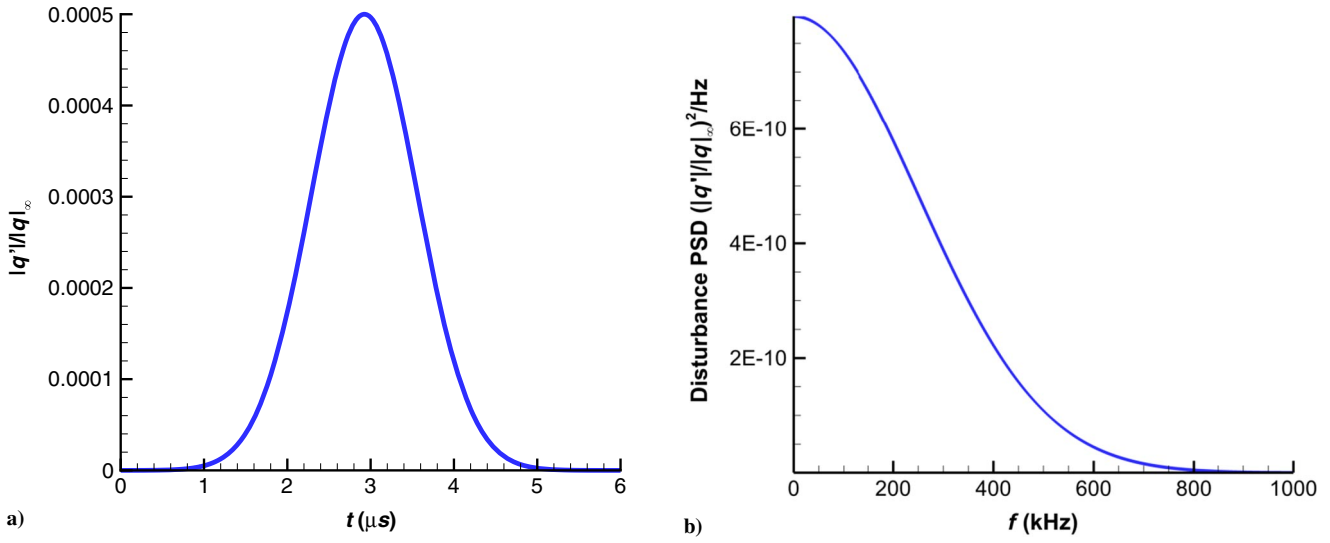

Fig. 3 Freestream disturbance distributed over a) time and b) frequency for axisymmetric pulse.

procedure to Ma and Zhong [4] and Huang and Zhong [9], the local growth rates for each frequency are determined by

$$-\alpha_i = \frac{1}{|H(f_n)|}\frac{d|H(f_n)|}{ds} \tag{14}$$

and the local wave numbers are determined by

$$\alpha_r = \frac{d\phi_n}{ds} \tag{15}$$

where s corresponds to the local streamwise coordinates and ϕ_n is the disturbance phase angle of the n th frequency. The phase speed of a given disturbance at a given frequency is defined as

$$c_r = \frac{2\pi f_n}{\alpha_r} \tag{16}$$

The response of the system to each freestream disturbance environment can be represented through a receptivity coefficient. This receptivity coefficient $C_{\text{rec}}(f)$, defined here as the initial amplitude of the second mode disturbance at the branch I neutral point for a discrete frequency f to freestream forcing of the same frequency, is determined using a combination of LST and unsteady DNS data. In the presence of a strong second mode it is assumed that the receptivity coefficient can be extracted by reconfiguring the N-factor relation, as shown in Eq. (17).

$$C_{\text{rec}}(f) = A_0(f) = \frac{A(s^*, f)}{e^{N(s^*,f)}} \tag{17}$$

Here $A(s^*, f)$ is the Fourier decomposed surface pressure normalized by the freestream disturbance and $e^{N(s^*,f)}$ is the exponentiated N-factor determined through LST for a given frequency f and a streamwise location s^*. The nondimensional amplitude $A(s^*, f)$ for the acoustic and entropy disturbances is derived by normalizing the local surface pressure perturbation at a given frequency by the freestream density perturbation of the same frequency in the freestream pulse $|d\rho_\infty(f)/\rho_\infty|$. For the vorticity pulses, this instead uses the freestream velocity disturbance $|dv_\infty(f)/a_\infty|$, as no density perturbations are imposed in the freestream. This normalization is based on the relative peak amplitude ϵM_∞ from the dispersion relations in Eqs. (9–12), and accounts for the nonuniform frequency distribution of disturbance amplitudes in the freestream pulses. The N-factor and perturbation data are sampled at the same streamwise position. It is observed later that the choice of sampling location does have some influence on the resulting receptivity coefficients due to the influence of freestream forcing.

IV. Steady Flowfield Solution

The steady DNS pressure and temperature mean flow contours for the cone are shown in Fig. 4a near the nose region and in Fig. 4b throughout the entire computational domain. A total of 240 points were used in the η direction, whereas the distribution in ξ ranged from 30 points per mm at the nose to 5 points per mm at the end of the geometry. These distributions were chosen to ensure that sufficiently large wavenumber disturbances could be captured by the simulation and to provide sufficient resolution in the mean flow data so as to reduce numerical inconsistencies in the LST analysis. A total of 10,080 points were used in the ξ direction to resolve the cone to 1.9 m. Marineau et al. [26] studied cones up to lengths of 1.5 m. The domain here was lengthened to allow for the development of a more amplified second mode that would be used to generate spectral receptivity data for the studied pulse disturbances.

The temperature contours in Fig. 4a depict a broad temperature gradient in the frustum region immediately after the nose. This is indicative of a similarly extensive entropy gradient and is representative of the generation of a significant entropy layer as expected for this relatively blunt nose. Figure 4b similarly shows a significant surface normal temperature gradient extending far downstream from the nose and indicates that the entropy layer is not swallowed for a large portion of the computational domain. These entropy layers reduce local flow velocities and density, and in turn reduce local Reynolds numbers. Because transition locations have been correlated with larger local Reynolds numbers, this process has been used to explain the transition delaying mechanism for intermediate nose bluntness [36]. However, this fails to explain transition reversal effects observed in large bluntness flows [33]. Zhong and Ma [16] observed the emergence of an additional generalized inflection point in the entropy layer of their blunt cone, which may be indicative of inviscid instability. These entropy layer instabilities can be absorbed by the boundary layers in blunt cones and potentially lead to early transition, though they have been observed to be relatively weak in perfect gas flows. They also pointed out that nonmodal instabilities may have stronger influence in blunt cones, and cause this reversal. Balakumar and Chou [19] also observed large oscillations in the entropy layer before second mode disturbances eventually began to dominate further downstream on their straight blunt cone cases. Further investigation of the effects of freestream receptivity in the entropy layer may be of interest in resolving this problem.

The wall-normal profiles of both velocity and entropy are presented in Fig. 5. The velocity profiles in Fig. 5a demonstrate weak variation in boundary-layer height after approximately $s^* = 0.7405$

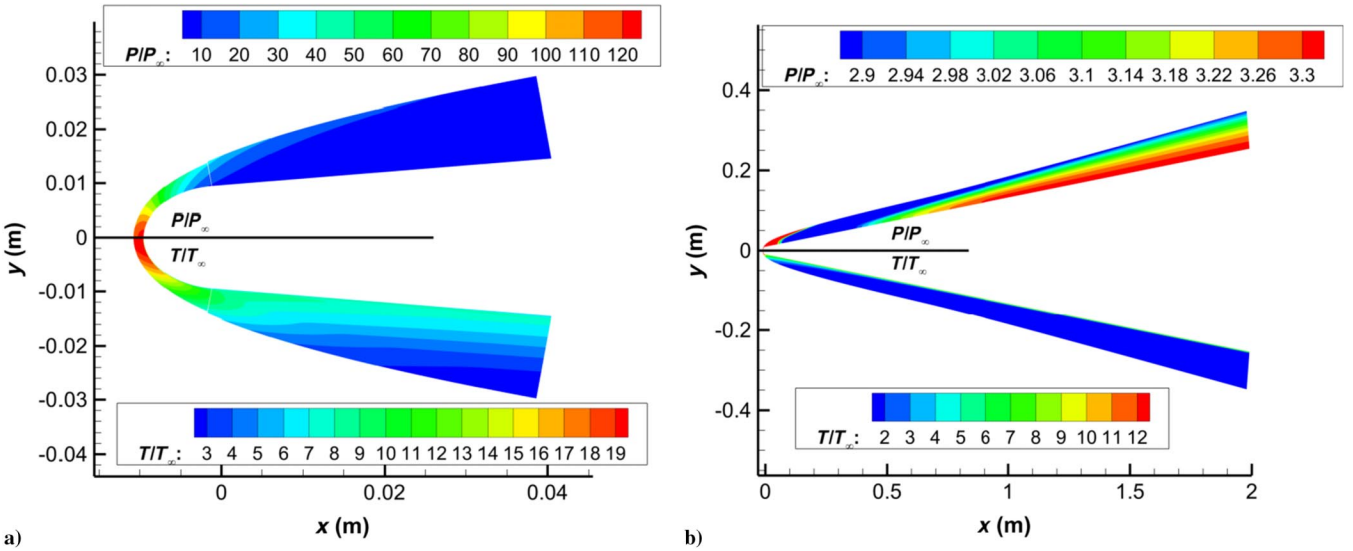

Fig. 4 Partial view of pressure (top) and temperature (bot) contours for a) the nose region and b) the entire cone.

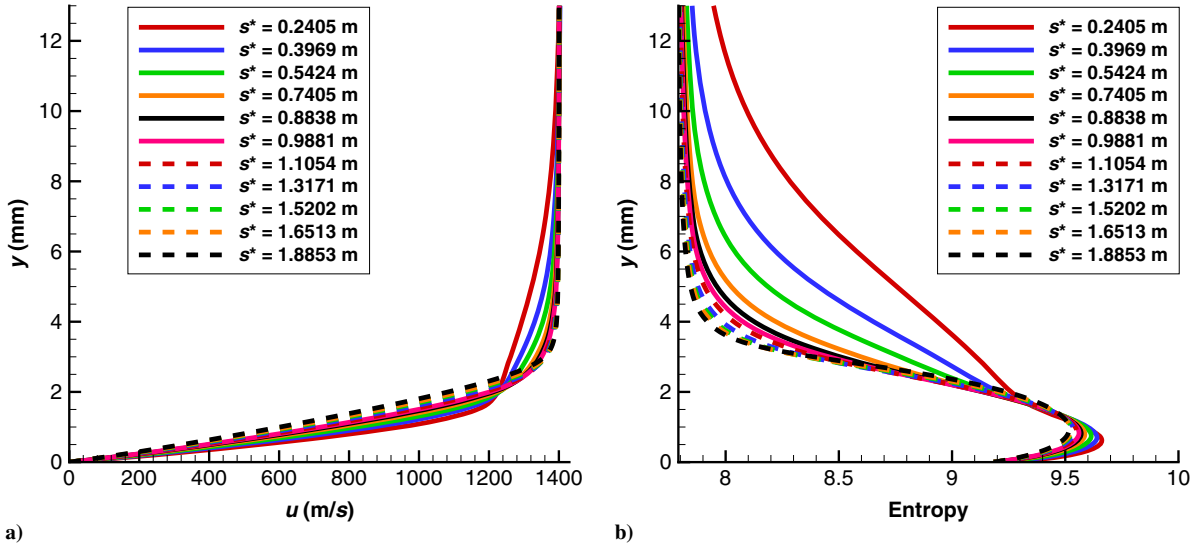

Fig. 5 Wall-normal a) U velocity and b) S entropy profiles at different positions along the cone.

m. The extent of the entropy layer is defined in Fig. 5b, in which it is shown to extend above the boundary layer across much of the cone. The entropy layer and boundary layer are observed to merge near approximately $s^* = 0.9881$ m, after which both the velocity and entropy profiles experience relatively minor variation in the streamwise direction. While the more extensive entropy profile variation before $s^* = 1$ m indicates potential nonparallel effects in the thermal boundary layer up to this point, it was found that the modal disturbance amplification profile does not vary much when taking nonparallelism into account for this case. Thus, a locally parallel assumption was used in the linear stability analysis for this study.

The convergence of the mean flow used in this study is discussed in detail by He and Zhong [37], where grid independence was verified using the current 240 point$j$ grid and a doubled 480 point$j$ grid. The difference between the original and refined grids is quantified by the infinity norm of the relative error, which is defined as the maximum error in the temperature or velocity profile. The infinity norm based on the velocity was found to be 1.65×10^{-6}.

V. LST Results

LST results indicate a strong amplified second mode band between frequencies of 118 and 238 kHz. At the reported experimental transition location of 1.037 m for this case [26], the unstable second mode is found between frequencies of 150 and 185 kHz and compares well to Marineau's results. The growth rate contours and the neutral stability curve are shown in Fig. 6. The neutral stability curve was generated by fitting the branch I and branch II neutral stability points and is highlighted in black. In this figure positive $-\alpha_i$ growth rates inside the curve correspond to the unstable second mode region.

The N-factor of the discrete frequency disturbances can be calculated using Eq. (6) to integrate the growth rates in the streamwise direction. The results of this analysis are depicted in Fig. 7. A direct comparison between the selected discrete frequency LST N-factors as shown in Fig. 7a, and Marineau's Parabolized Stability Equation (PSE) derived N-factors are shown in Fig. 7b. The lines in Fig. 7b are made by fitting the curve profiles for each of the sampled LST frequencies.

For this case (corresponding to Run 3752), Marineau et al. [26] reported an experimentally determined transition location of $s = 1.037$ m, along with a corresponding N factor of 1.6. The LST results of this study report an N-factor of approximately 1.7 at the experimental transition location and are consistent with Marineau's results for this case. In general, the LST results correlate reasonably well with the PSE data reported by Marineau, with our LST overpredicting the N-factors slightly throughout the downstream sections of the domain. This difference can be attributed to nonparallel effects that the LST formulation neglects compared with the PSE algorithm

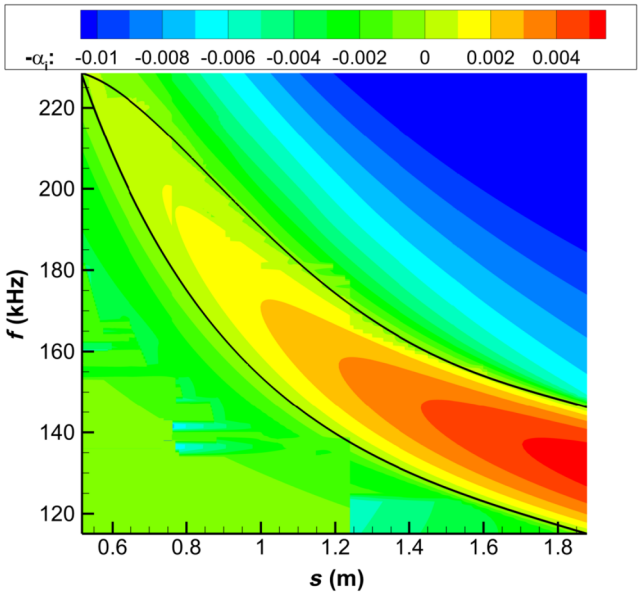

Fig. 6 LST growth rate contour and neutral stability curve.

used by Marineau. While nonparallel effects seem to have the most effect on higher frequency disturbances upstream on the cone, the primary amplification behavior matches remarkably well with Marineau's reported results and indicate that the most dominant modal disturbances for this case are not too strongly affected by boundary-layer variation.

The phase speed and growth rate of the 150 kHz disturbance are presented in Fig. 8 and are used later to validate the unsteady DNS results. This disturbance frequency was chosen because it was observed to contain a highly amplified second mode. It is shown that the primary second mode disturbance corresponds to the discrete mode F emerging from the continuous fast acoustic spectrum. The continuous spectra are indicated in the phase speed plot by the dashed lines at $1 + 1/M_\infty$ for the fast acoustic, 1 for the entropy/vorticity, and $1 - 1/M_\infty$ for the slow acoustic modes. Additionally, Fig. 8 shows that this particular frequency demonstrates an extensive synchronization region between mode F and mode S, lying between 1.1 and 1.7 m along the cone.

VI. Unsteady DNS Results

The receptivity of the cone was studied in response to a variety of broadband, continuous frequency spectra freestream disturbances. To do this, the pulse disturbances described in Sec. III.C were introduced analytically in the freestream. These pulses were advected along the central axis of symmetry in the streamwise direction over the mean flow. The resulting boundary-layer disturbances on the cone's surface were decomposed with FFT into their spectral frequency components. The specific disturbance cases and their respective labels are given in Table 3. The disturbances are differentiated by both their freestream perturbation type and their geometry. The fast acoustic, slow acoustic, temperature (entropy), and vorticity disturbances are defined by the freestream dispersion relations in Eqs. (9–12), respectively. The freestream spectra of the pulses were fixed to be the same within the finite spherical and planar cases, respectively.

A. Finite Spherical Pulse Unsteady DNS Results

Figure 9 depicts the instantaneous pressure and temperature disturbances immediately after the finite pulse interaction at the nose for case B1. The pressure disturbance in Fig. 9a depicts acoustic waves propagating toward the cone surface and being reflected back toward the bow shock. The temperature disturbance in Fig. 9b on the other hand depicts temperature perturbations moving at the local flow velocity and piling up, not experiencing the reflection associated with acoustic waves. These are indicative of excited entropy modes and are very similar to the structures that Huang and Zhong [9] observed for their entropy spot study. Similarly, Fig. 10 for the finite spherical fast acoustic pulse (case B1) shows the pressure and temperature disturbance contours at a downstream position on the cone. The rope-like wave structures in the temperature profile in Fig. 10b are indicative of a perturbation growing in accordance with Mack's second mode [4]. These leading-edge and boundary-layer disturbances were qualitatively observed in each case considered in this study and indicate strong second mode amplification downstream on the cone.

In addition to the conventional second mode, Mach wave-like radiating structures can be observed near the tail end of the disturbance wave packet, most prominently for the pressure disturbances in Fig. 10a. This behavior is characteristic of a supersonic mode, in which the phase speed of the disturbance is supersonic with respect to the mean flow [38]. Recent studies have shown that these supersonic modes may have disturbance amplitudes similar in strength to second mode instabilities, and as a result may be of significant importance in the process of transition for real gas flows [38–41]. However, similar to Reshotko [2] the supersonic modes observed here are relatively weak and occur downstream enough that they are unlikely to significantly affect transition. A wider consideration of their effects on stability and their general receptivity response may also be of interest for future work.

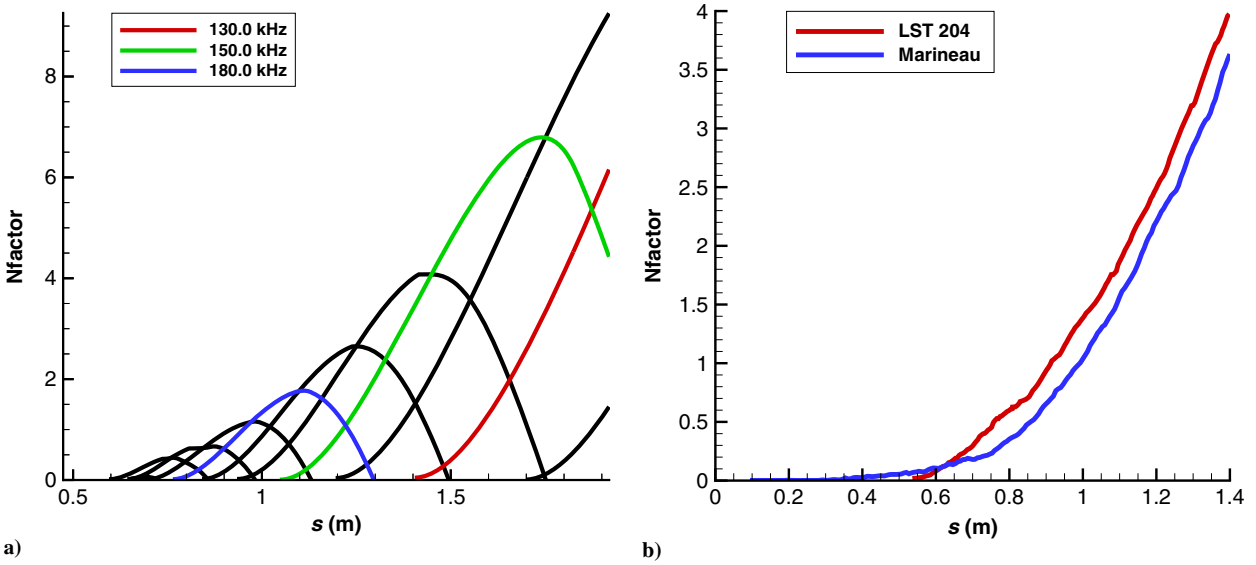

Fig. 7 a) *N*-factor data ranging between 120 and 220 kHz with $\Delta f = 10$ kHz. b) Current LST *N*-factors vs Marineau's [26] reported PSE *N*-factors.

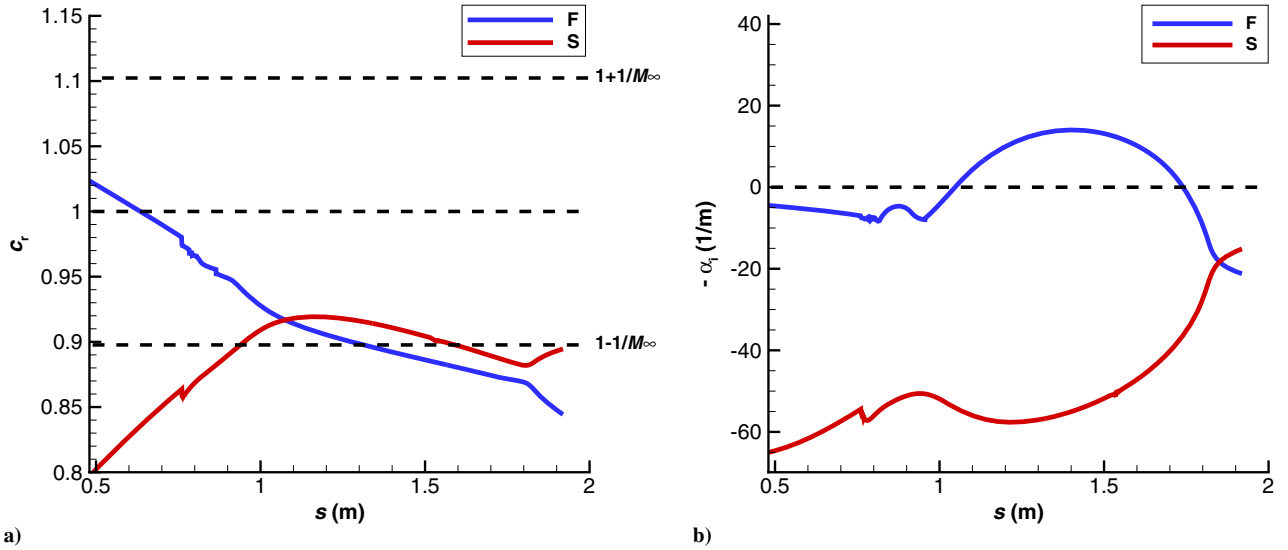

Fig. 8 Streamwise LST results at $f = 150$ kHz for a) phase speed and b) growth rate.

Table 3 Freestream disturbance cases for unsteady DNS

Disturbance type	Case
Finite spherical fast acoustic	B1
Finite spherical slow acoustic	B2
Finite spherical temperature	B3
Finite spherical vorticity	B4
Planar fast acoustic	B5
Planar slow acoustic	B6
Planar temperature	B7
Planar vorticity	B8

The normalized surface pressure perturbations resulting from the finite spherical fast acoustic pulse (case B1) are presented in Fig. 11 for a selection of streamwise positions. Before the second mode region, the wave packet is complex in shape and is dominated by oscillations associated with nonmodal forcing. These forcing waves are shown to decay upstream of the second mode region before experiencing significant amplification as they propagate downstream. A more regular waveform appears after $s^* = 1.42$ m and is observed to experience exponential amplification in its magnitude as it propagates downstream. This is indicative of a dominant second mode instability.

The total surface disturbances depicted in Figs. 10 and 11 may be studied more quantitatively through the use of Fourier decomposition (FFT). The resulting normalized spectral surface pressure contour maps for the finite spherical fast acoustic (case B1), slow acoustic (case B2), temperature (case B3), and vorticity (case B4) disturbances are shown in Fig. 12. Again, these Fourier decomposed pressure disturbances are normalized by the spectral content of the initial freestream disturbance shown in Fig. 3b to account for the nonuniform frequency distribution of the initial pulse [22]. Additionally, the LST neutral curve is also plotted in solid black lines in these figures in order to validate the unsteady simulation. The most amplified frequency was observed to be between approximately 140 and 150 kHz and agrees well with the LST *N*-factors results presented previously. The neutral curves align as expected with the instability band, because peak unsteady amplification for the second mode disturbance should be centered about the branch II neutral line [38]. Although there is a slight offset between the maximum amplitude of the second mode amplification lobe and the branch II curve, this is attributed to the nonparallel effects disregarded by the LST calculations. However, it is observed later in Fig. 15 for the 150 kHz disturbance that these nonparallel effects are very miniscule, and our DNS and LST demonstrate close agreement at the peak disturbance frequencies. Thus, although LST does not account for freestream forcing or nonparallel effects, the resultant downstream perturbation spectra are shown to be dominated by the modal instability predicted

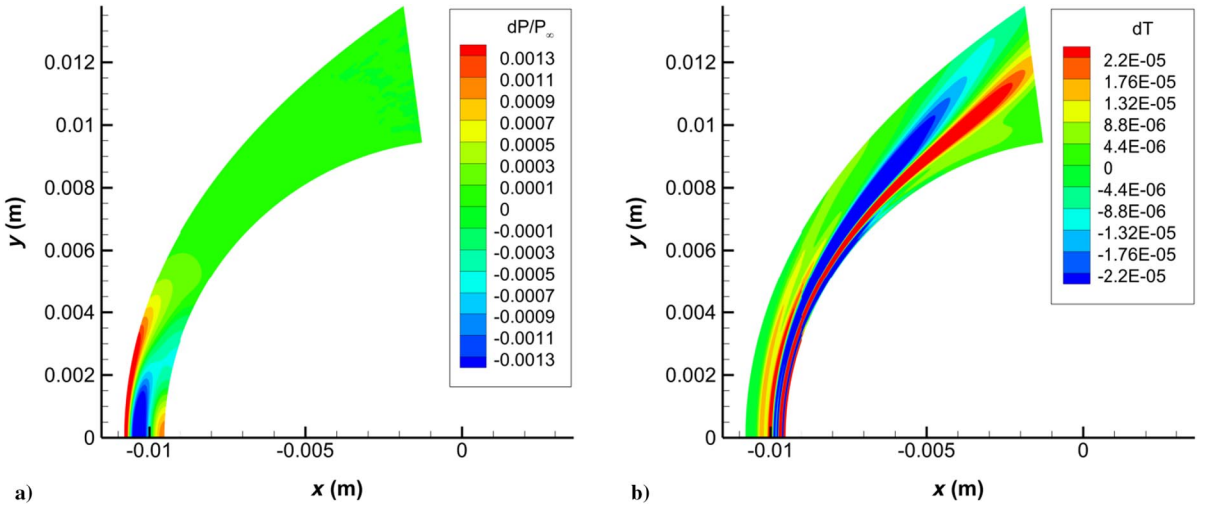

Fig. 9 a) Pressure and b) temperature perturbations at the nose region after the finite spherical fast acoustic perturbation (case B1).

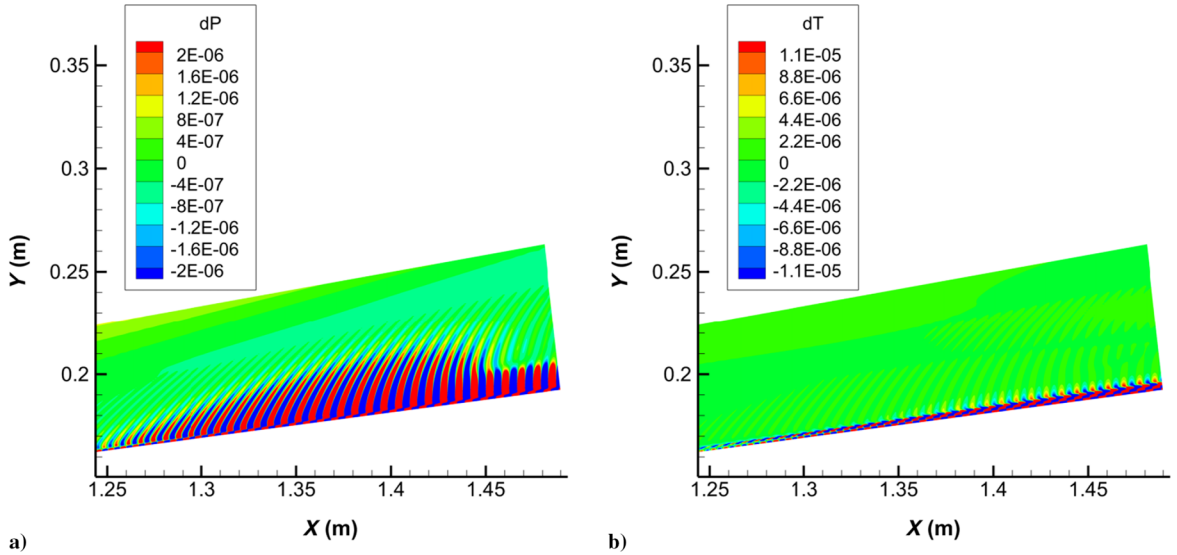

Fig. 10 a) Pressure and b) temperature perturbations near $s^* = 1.5$ m after the finite spherical fast acoustic perturbation (case B1).

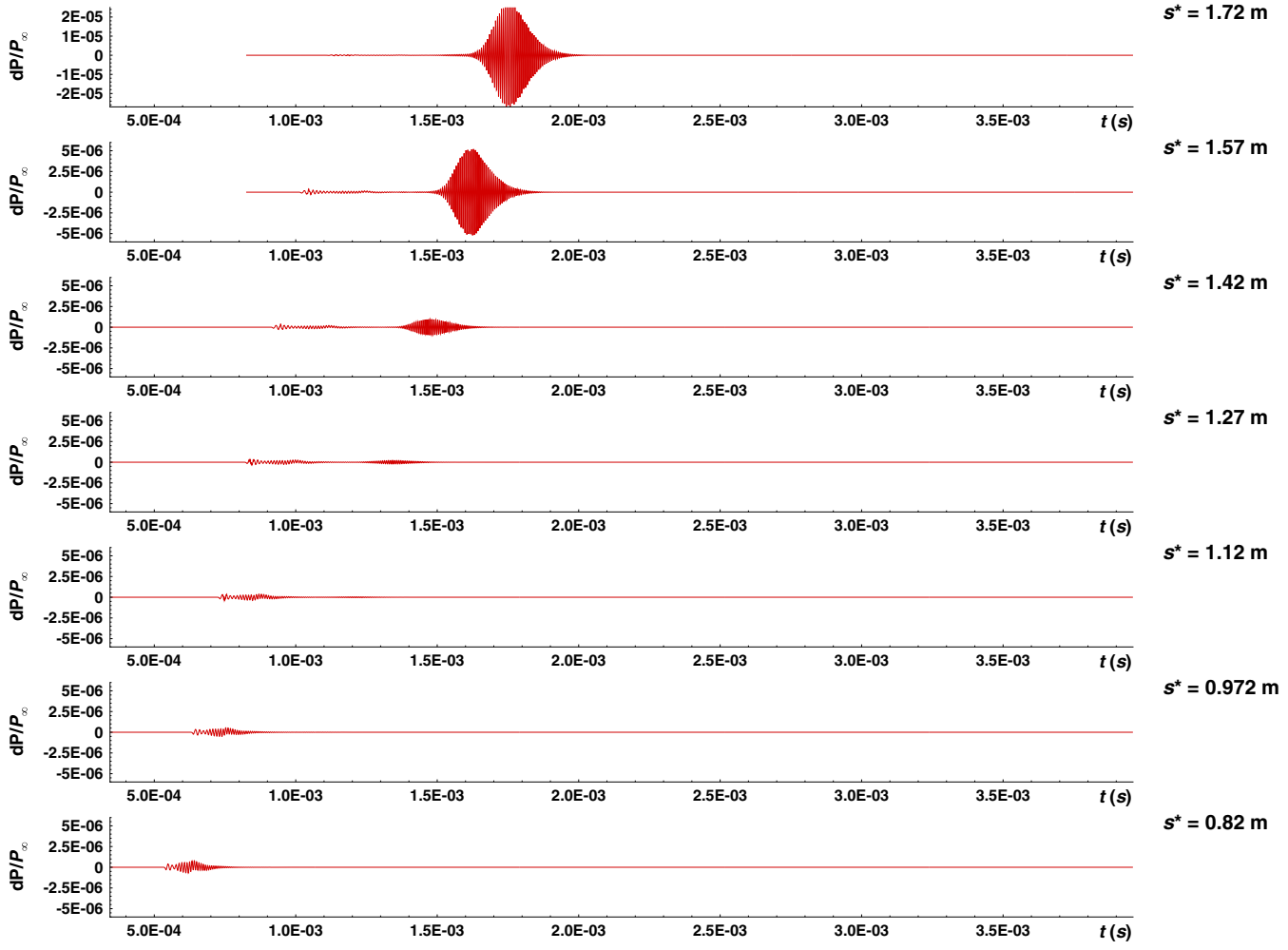

Fig. 11 Time history of normalized surface pressure perturbations resulting from finite spherical fast acoustic pulse disturbance (case B1).

by LST and the LST results are still relevant to the amplification behavior of the primary flow instability.

From Fig. 9 it is seen that case B1 excites significant acoustic and entropy/vorticity disturbances at the leading edge of the cone. The complex interactions and acoustic reflections at the nose generate the initial perturbations that force the boundary layer. Additionally, the large bluntness of the cone indicates the presence of a significant entropy layer, through which additional instabilities may be produced and propagate to force the boundary layer. This is likely observed in Fig. 12 as the pulses induce upstream disturbances between 100 and 200 kHz. This excitation gradually dampens in the streamwise direction until second mode growth generates the red

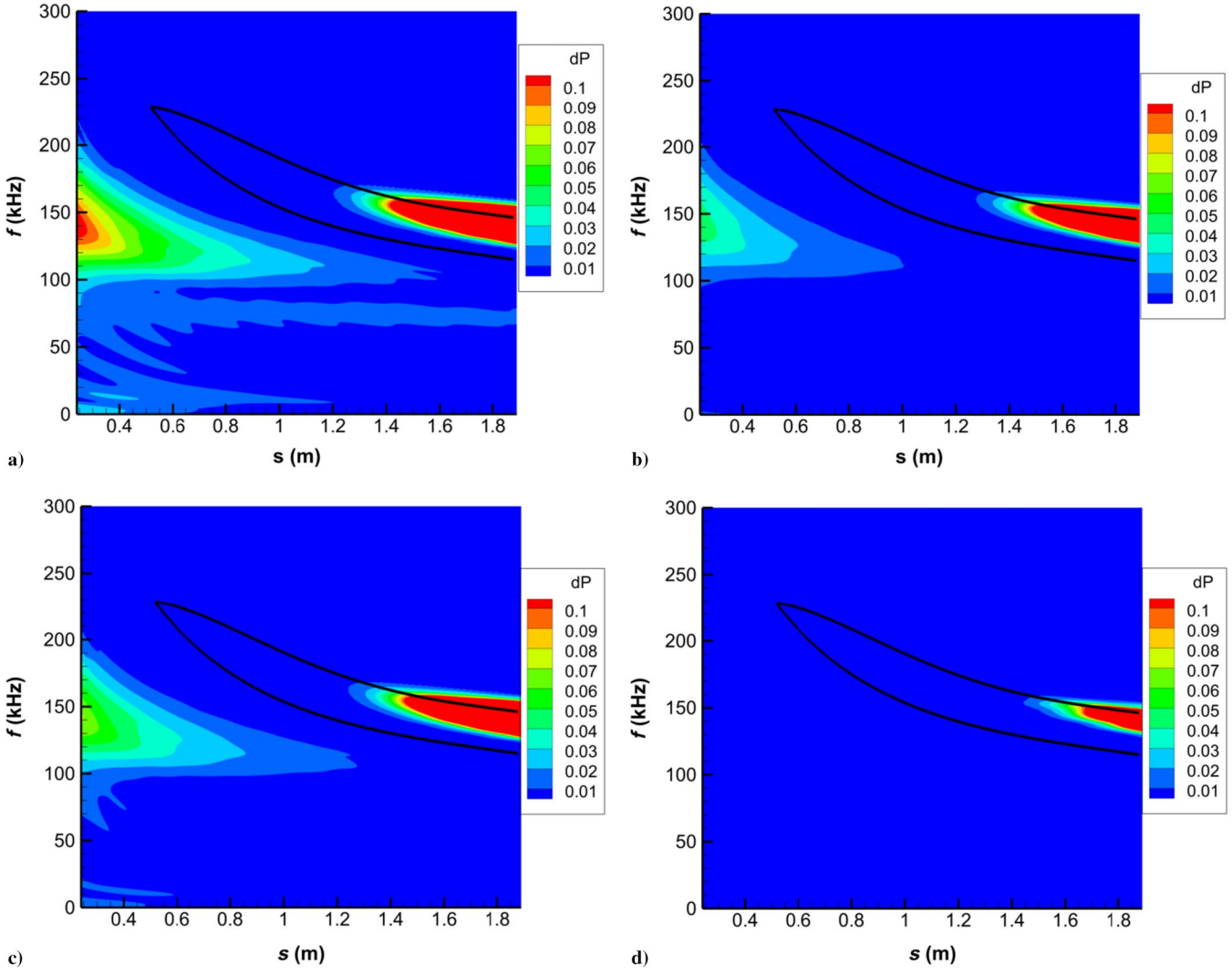

Fig. 12 Surface FFT pressure distribution for a) case B1, b) case B2, c) case B3, and d) case B4.

lobe seen at the end of the computational domain in all four cases. A similar phenomenon is observed in all of the finite pulse cases, though the general receptivity of the mean flow to freestream vorticity disturbances is weak enough that this forcing cannot be seen in the uniform contour levels in Fig. 12d for case B4. The primary band of instabilities observed in all four cases is centered between approximately 140 and 170 kHz, depending on streamwise position and corresponds to the most highly amplified second mode disturbance frequencies. Both the initial forcing and the second mode disturbance amplitudes were strongest for the finite spherical fast acoustic disturbance (case B1), followed by the temperature (case B3), the slow acoustic (case B2), and finally the vorticity (case B4) disturbances, respectively.

The spatial development of surface pressure perturbation amplitudes for a selection of highly amplified second mode frequencies is given for case B1 in Fig. 13. The results for the other finite pulse cases are very similar and are omitted for concision. In the plot, each of the sampled frequencies initially start with significant amplitudes associated with the boundary-layer perturbations initially excited upstream at or near the leading edge of the cone. Similar to what was observed in Figs. 11 and 12 these disturbances are attenuated until second mode amplification takes hold downstream. The oscillations in these signals are indicative of modal interference effects, which can be observed near the local minima of each frequency. This particular point is attributed to the synchronization between the different modal disturbances. The 160 and 170 kHz sampled frequencies also exhibit the modal oscillation behavior near the end of the domain, which is indicative of interactions with higher

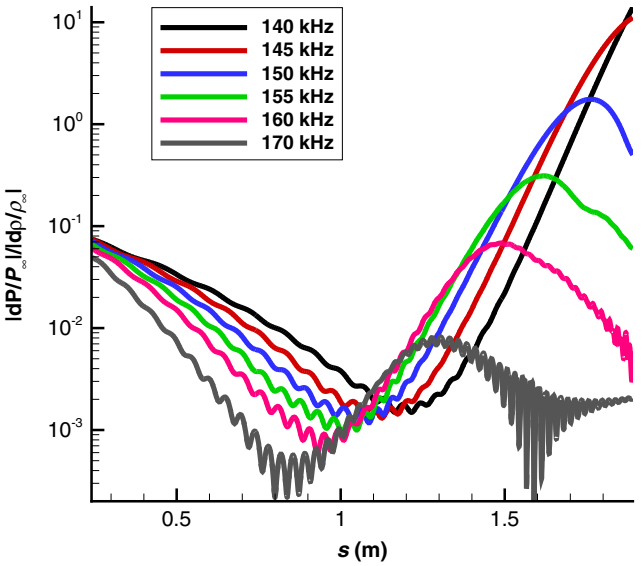

Fig. 13 Normalized surface pressure disturbance amplitudes for selected second mode frequencies for case B1.

disturbance modes. The 155 kHz disturbance also demonstrates a distinct kink near $s^* = 1.7$ m that shows some minor localized amplification not observed for the other disturbance frequencies.

Similar discontinuities have been observed in growth rate curves by Knisely and Zhong [38] for supersonic mode instabilities.

The FFT decomposed surface pressure perturbations at different streamwise locations are also presented in Fig. 14 for cases B1–B4. As expected, the spectral surface pressure distributions for the finite spherical cases are very similar to each other. Again, we see that case B1 excites the strongest overall pressure perturbations downstream in the second mode region. Case B1 also generates stronger initial disturbance waves upstream of the second mode amplification region similar to the behavior observed in the normalized surface pressure contours. Distinctive peaks in the disturbance amplitude can also be seen here, initially centered around frequencies of approximately 170–180 kHz. As the sampling point moves further downstream, this peak disturbance band shifts to center around lower frequencies while also growing in overall amplitude, eventually centering around 145–155 kHz near the end of the computational domain. The amplitude peaks observed here correspond to the primary second mode instability for this flow and their behavior corresponds well to the LST results in Fig. 6, as maximum second mode amplitudes are expected to follow with the branch II neutral point. The broadband disturbance dampening and amplification pattern is clearly seen again here. While the disturbance amplitudes for cases B2, B3, and B4 are smaller, the same general trends are observed.

Through Eqs. (14–16) the FFT decomposed unsteady DNS can be used to calculate the growth rates and phase speeds of different discrete frequency surface perturbations. The 150 kHz frequency disturbance in particular was used in order to validate the results of the unsteady DNS. The results for the 150 kHz frequency disturbance for the finite spherical fast acoustic (case B1) are presented in Fig. 15.

The unsteady DNS results for case B1 show good agreement with LST, demonstrating that the discrete mode F is unstable for this case. The signal for this case, and for the other finite pulse cases, show that the boundary-layer disturbances are dominated by mode F disturbances upstream on the cone. This indicates that the initial nose excitations primarily force discrete fast acoustic disturbances for all the finite pulse cases, similar to what Huang and Zhong [9] observed for an entropy pulse. The LST predicts an extensive synchronization range for this frequency between streamwise locations of 1.1 and 1.8 m. Near the beginning of the synchronization region, significant oscillations in both the phase speed and growth rates can be observed in the DNS results. This oscillation is indicative of modal interference associated with the synchronization of the discrete modes, though it is still apparent that the newly destabilized mode F dominates. These oscillations dampen out significantly as the disturbance propagates through the end of the domain for case B1 in Fig. 15. Nearly identical responses are observed as well for cases B2, B3, and B4 and as such are relegated to Supplementary Figs. S1, S2, and S3, respectively. In all of the finite spherical pulse cases it was shown that the pulse disturbances generated significant discrete mode F waves in the boundary layer upstream on the cone. After synchronization, the boundary-layer disturbance signal remains dominated by the unstable mode F predicted by LST.

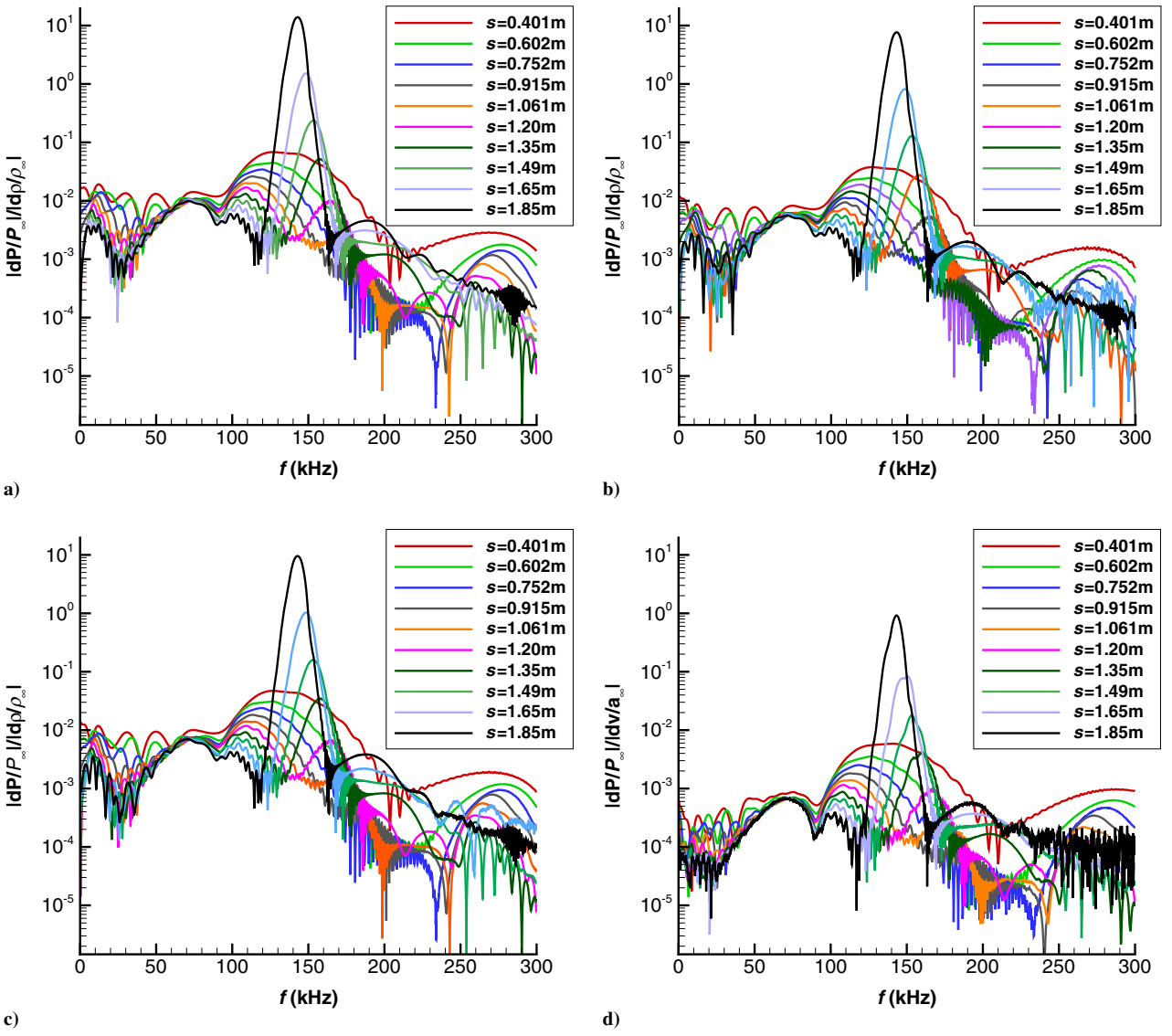

Fig. 14 FFT decomposed surface pressure spectra at various streamwise locations for a) case B1, b) case B2, c) case B3, and d) case B4.

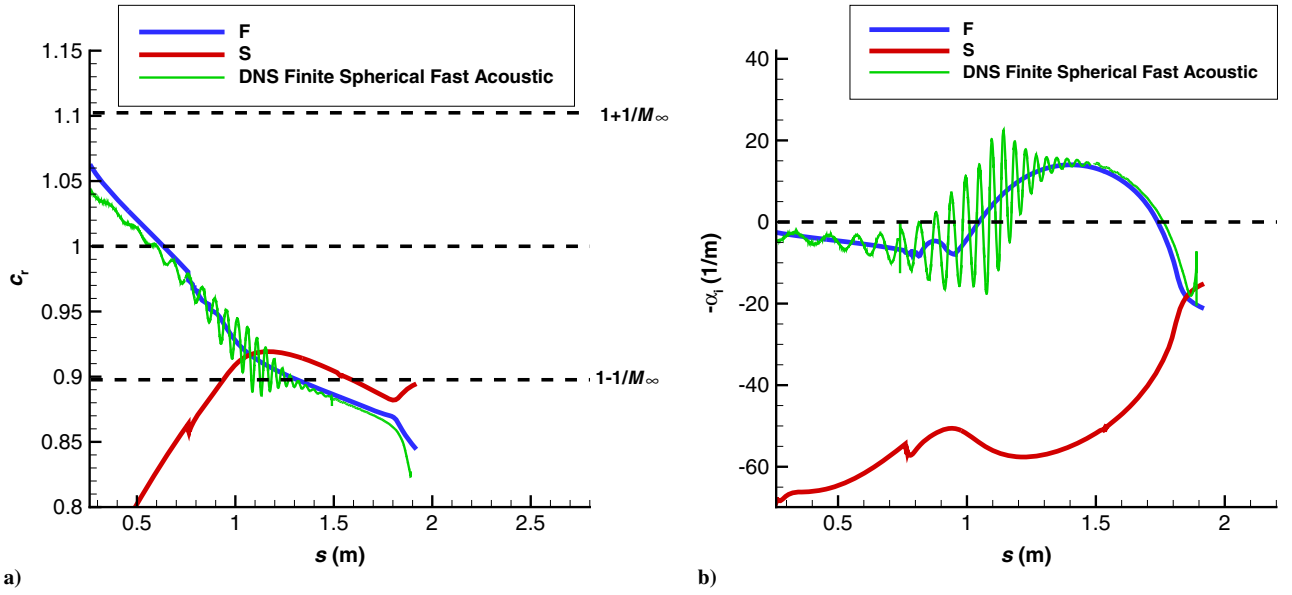

Fig. 15 Case B1 unsteady DNS vs LST predicted results for 150 kHz disturbances: a) phase speed and b) growth rate.

B. Planar Pulse Unsteady DNS Results

Figure 16 presents snapshots of the disturbance pressure contours resulting from the planar fast acoustic pulse (case B5) over a downstream region of the cone at two different instances. Because the planar pulses are infinite in the y–z plane, they continuously interact with and introduce forcing to the shock layer as they propagate in the streamwise direction. In particular, Fig. 16a depicts the front of the downstream shock–disturbance interaction and the wake of disturbances it excites, whereas Fig. 16b shows the slower band of amplifying second mode disturbances behind the pulse front. In Fig. 16a a sharp interface can be seen at the leading edge of the disturbance front at $x = 1.46$ m and is attributed to continuous fast acoustic disturbances that are generated in the shock layer by the shock–disturbance interactions. This distinctive edge propagates with the speed of the acoustic pulse and shows significant forcing being generated by the disturbance that directly interacts with the boundary layer. The result of this forcing can be observed in the normalized surface pressure time history plots in Fig. 17, which depicts a strong secondary disturbance spike caused by the planar forcing that propagates throughout computational domain. Trailing behind this leading waveform are additional perturbations distributed throughout the shear layer consisting of continuous spectrum disturbances propagating at their characteristic speeds. These include alternating sections of negative pressure disturbances between $x = 1.35$ m and $x = 1.45$ m and before $x = 1.28$ m, similar to what was observed by Huang and Zhong [9]. The secondary red structure near $x = 1.3$ m is associated with continuous slow acoustic modes, which also seem to be strongly amplified by the planar fast acoustic disturbance. The forced continuous modes seem to be very dominant for the planar fast acoustic case shown here. Even at a relatively downstream position of $s^* = 1.42$ m, the magnitude of the forcing disturbance overshadows that of the amplifying second mode disturbance wave packet. It is only near the end of the cone where the primary second mode disturbance begins to dominate. Furthermore, this forcing is also observed to experience amplification as it continues downstream, although much more weakly than the primary second mode. This amplification can also be explained by the continuous introduction of additional forcing throughout the domain by the planar pulse.

The second mode wave packet depicted in Fig. 16b somewhat follows the trends observed in the finite spherical disturbance cases. Clear isolated second mode structures can be identified in the boundary layer. A weak supersonic mode is again observed here for case B5, though it is shown to extend much farther into the shock layer. The other planar pulse cases were observed to have very similar

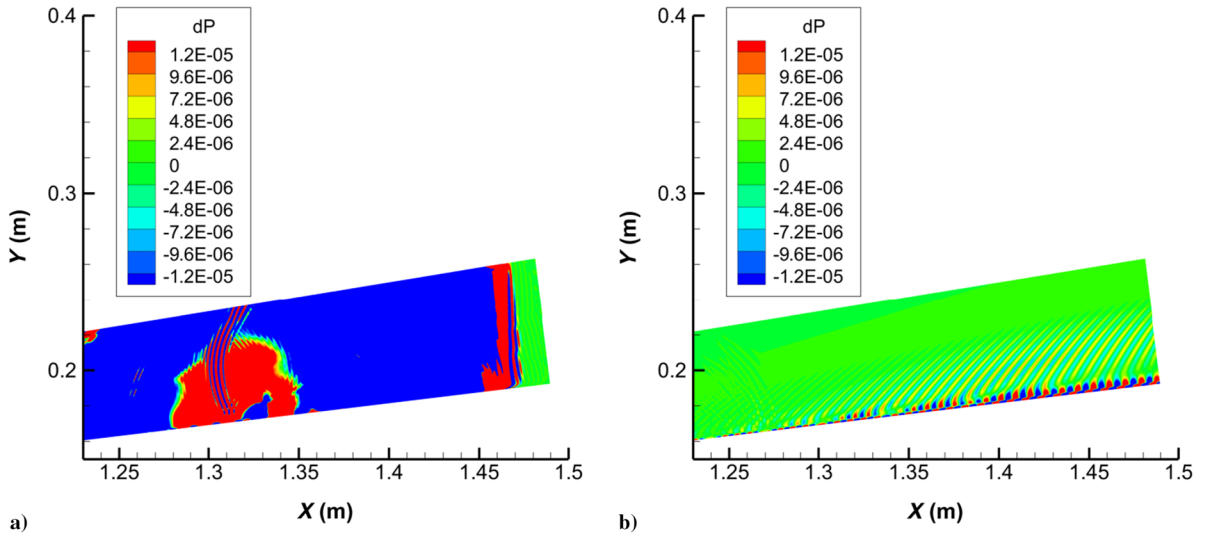

Fig. 16 Pressure perturbations near $X = 1.5$ m after the planar fast acoustic perturbation (case B5) for a) the pulse front shown beginning at $x = 1.46$ m and b) the primary second mode behind the pulse front.

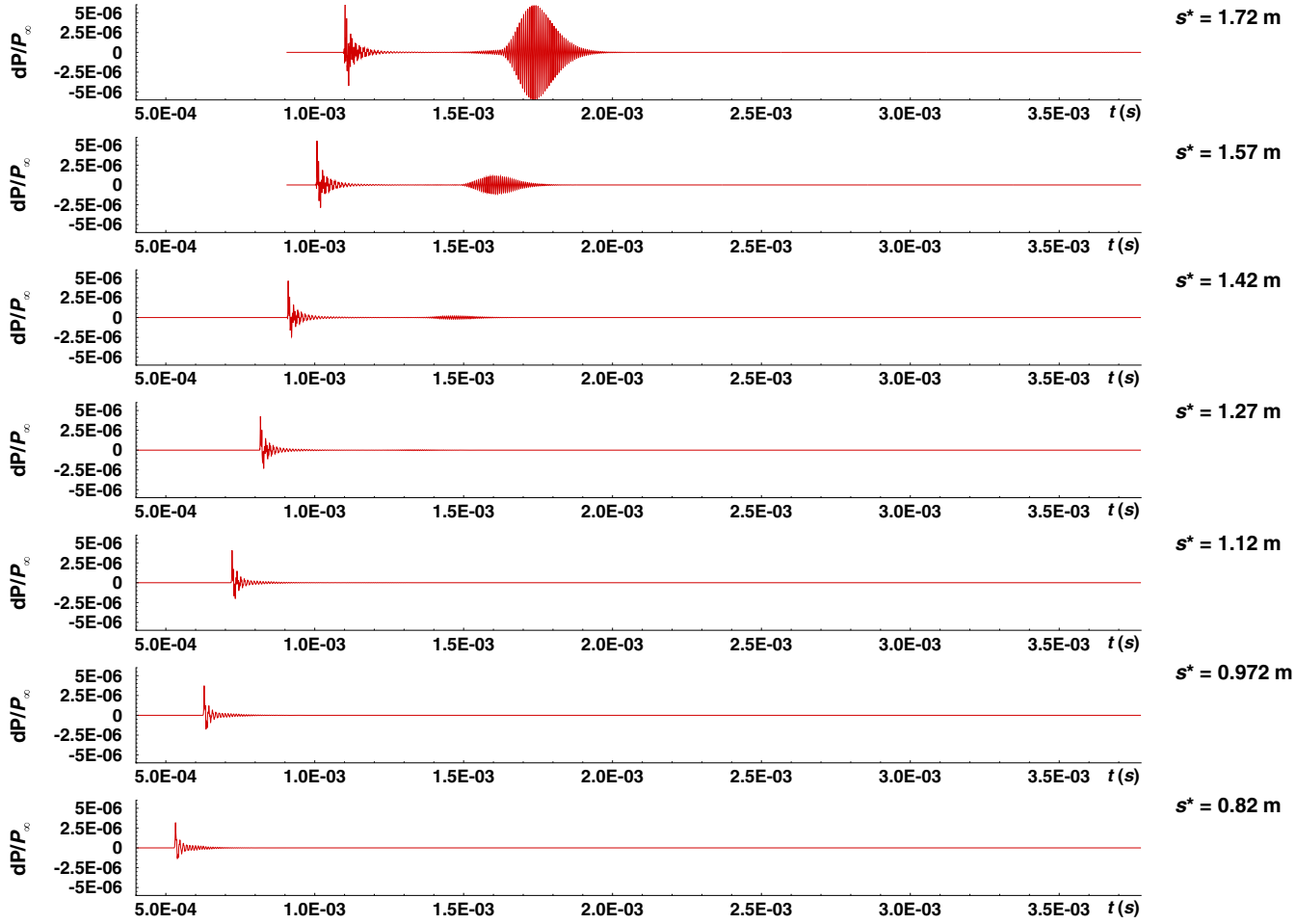

Fig. 17 Time history of normalized surface pressure perturbations resulting from planar fast acoustic pulse disturbance (case B5).

pressure contour and surface time history profiles to the finite pulse cases. These are depicted for the planar slow acoustic case B6 in the Supplementary Figs. S4 and S5.

The FFT decomposed surface pressure contour maps for the planar fast acoustic (case B5), slow acoustic (case B6), temperature (case B7), and vorticity (case B8) disturbances are presented in Fig. 18. The total surface disturbance spectra share many similarities to the finite spherical pulse cases. In particular, Fig. 18b for case B6 and Fig. 18c for case B7 depict strong initial forcing near the beginning of the domain that experiences limited attenuation compared with their finite pulse counterparts before second mode amplification. These lower frequency forcing waves remain much more significant in the downstream regions of the cone due to the continuous introduction of forcing from the planar pulses. Although noise effects are noticeably stronger for the planar cases, they are still observed to strongly excite primary second mode disturbances downstream on the cone and agree well with LST predictions.

The disturbance spectrum for case B5 in Fig. 18a is significantly more complex. A strong low-frequency disturbance band is still observed near 100 kHz, whereas another additional band of unstable frequencies between 180 and 260 kHz is also apparent. Contrary to the other cases, these additional disturbance bands seem to experience amplification as they propagate downstream through the domain, though the second mode is observed to have the highest amplitudes throughout. These additional disturbance bands may be continuous modes and other discrete modes that are excited by the continuous forcing input, and can be observed in the secondary wave packets in Fig. 17. Although these other instabilities are generally much weaker than the second mode for hypersonic flows [35,42] at the end of the cone, they may still have considerable impact on the flow. The presence of strong forcing and multimodal disturbances in the planar pulse cases necessitates the use of modal decomposition techniques in order to extract useful receptivity data for instabilities of particular interest, especially in noisy environments such as those considered in this study.

The spatial development of surface pressure perturbation amplitudes is plotted again in Fig. 19a for case B5 and in Fig. 19b for case B6. Cases B7 and B8 were very similar in structure to case B6 and are omitted. Case B6 demonstrates very similar general profiles to the finite pulses in cases B1–B4, though the lowest and most amplified frequencies in this case seem to experience minimal attenuation of the disturbances introduced upstream on the cone. Similar modal interference patterns and the distinct kink in the 156 kHz disturbance shown here are also observed, which indicate that higher disturbance modes and the supersonic mode may also play a further role in the downstream development of these disturbances. The results for case B5 show significantly weaker second mode amplification, though the upstream forcing levels are much higher than they are for case B6. Furthermore, these upstream disturbances experience little to no damping before second mode amplification, which indicates that the flow in this case is much more receptive to the forcing modes introduced by the planar fast acoustic pulse than the other unsteady pulse configurations.

The normalized surface pressure spectra at different streamwise locations for cases B5–B8 are shown in Fig. 20. Case B5 in Fig. 20a follows closely with the behavior observed in the finite spherical cases. However, the second mode amplitudes for case B5 are an order of magnitude smaller than those for case B6 in Fig. 20b and 30–50% smaller than those observed for case B7 in Fig. 20c and for case B8 in Fig. 20d. Cases B6–B8 share very similar low-frequency forcing structures outside of the second mode frequency band, whereas case B5 is observed to have significantly higher relative disturbance amplitudes outside of the second mode frequency range. In particular, a low-frequency band near 50–100 kHz and a

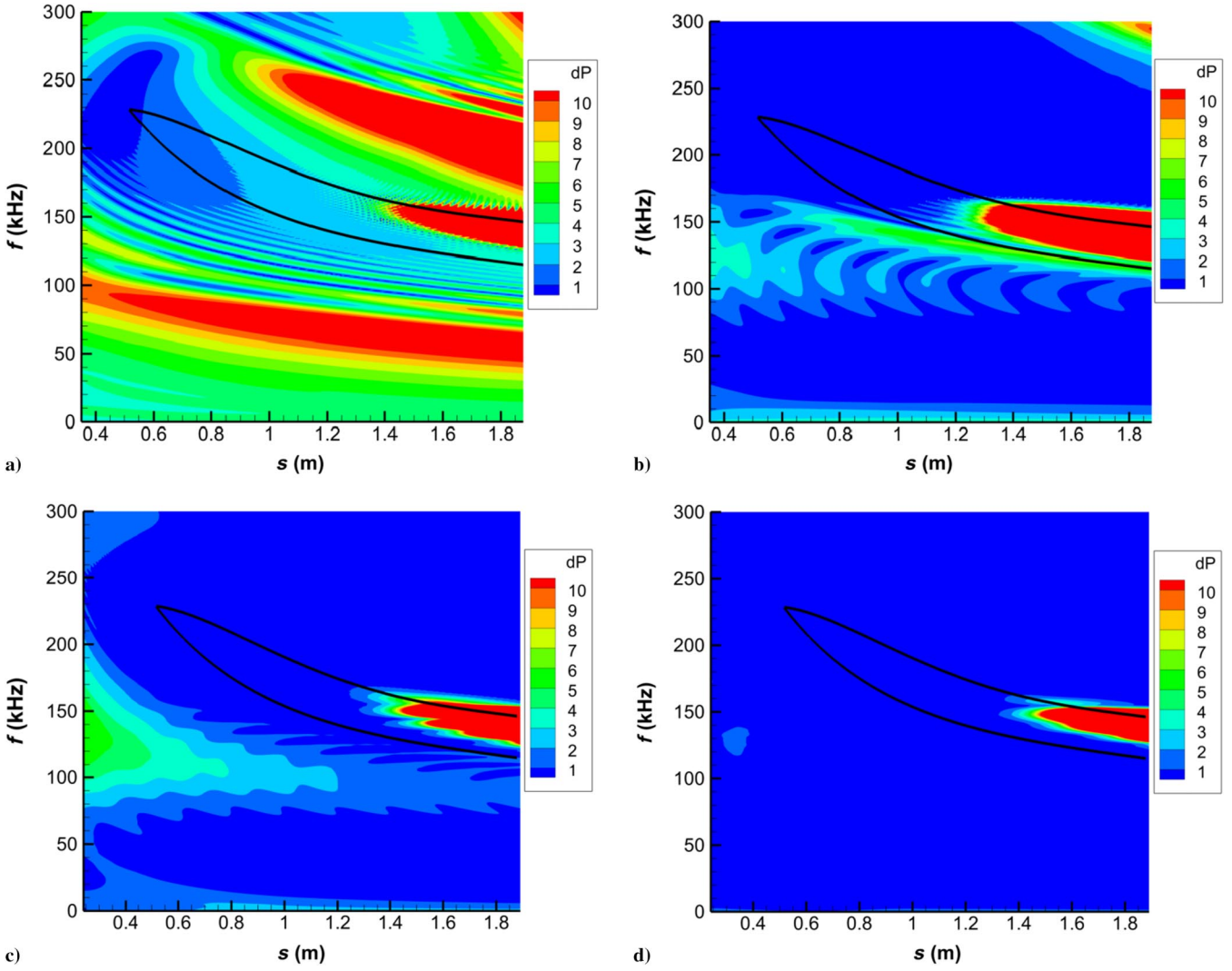

Fig. 18 Surface FFT pressure distribution for a) case B5, b) case B6, c) case B7, and d) case B8.

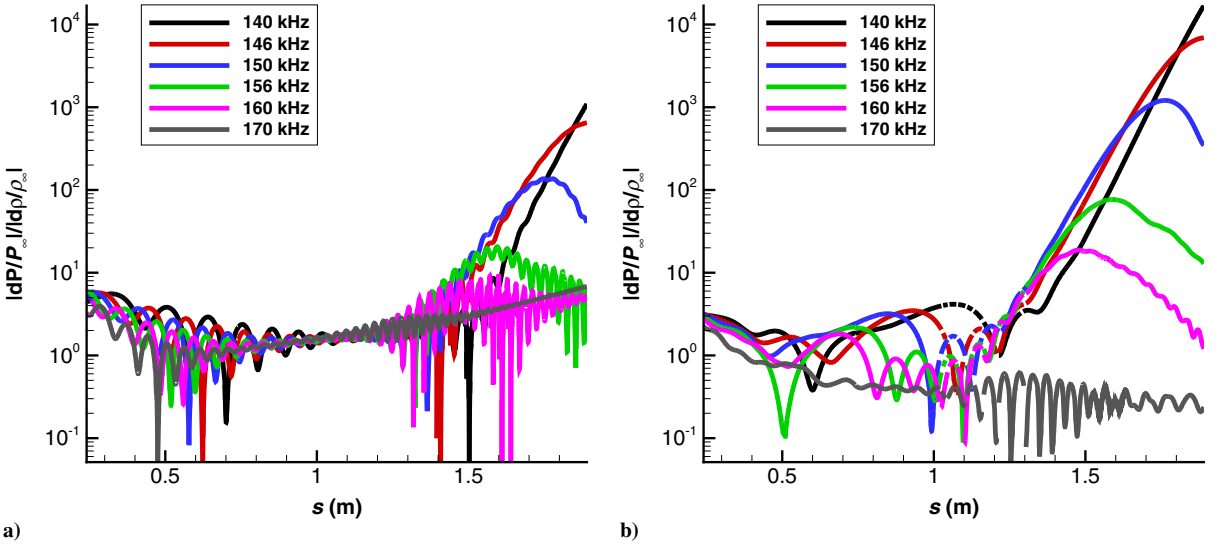

Fig. 19 Normalized surface pressure disturbance amplitudes of selected second mode frequencies for a) case B5 and b) case B6.

high-frequency band between 200 and 250 kHz are up to three orders of magnitude stronger for case B5. The higher frequency disturbance band is also shown to experience amplification as the disturbance propagates downstream in case B5. This indicates that the receptivity response for case B5 seems to distribute the forcing in a broadband manner, whereas cases B6, B7, and B8 primarily excite second mode waves.

This can be directly observed in the unsteady DNS versus LST phase speed and growth rate comparison in Fig. 21 for case B5. The boundary-layer disturbances resulting from case B5 do not seem to

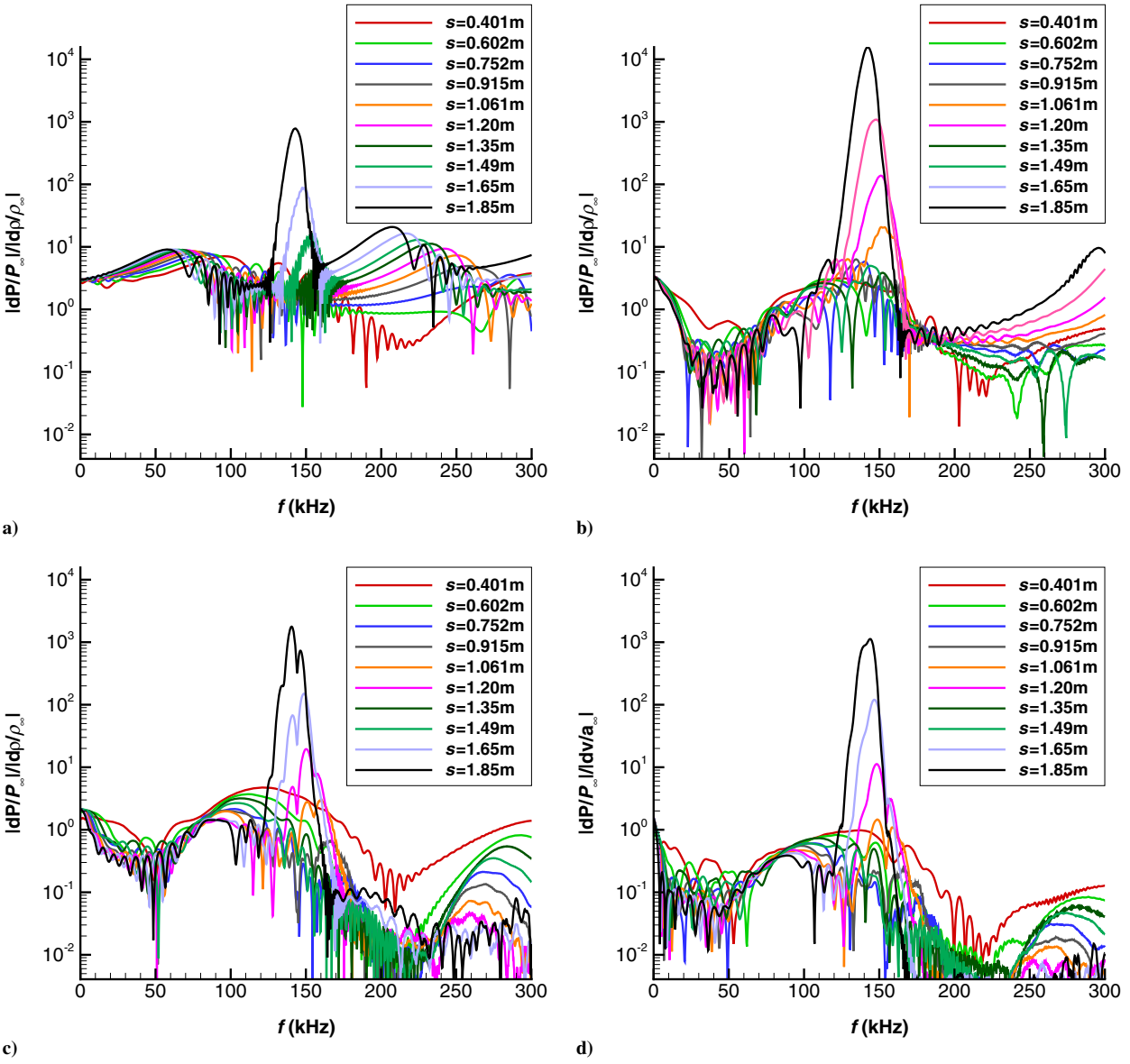

Fig. 20 FFT decomposed surface pressure spectra at various streamwise locations for a) case B5, b) case B6, c) case B7, and d) case B8.

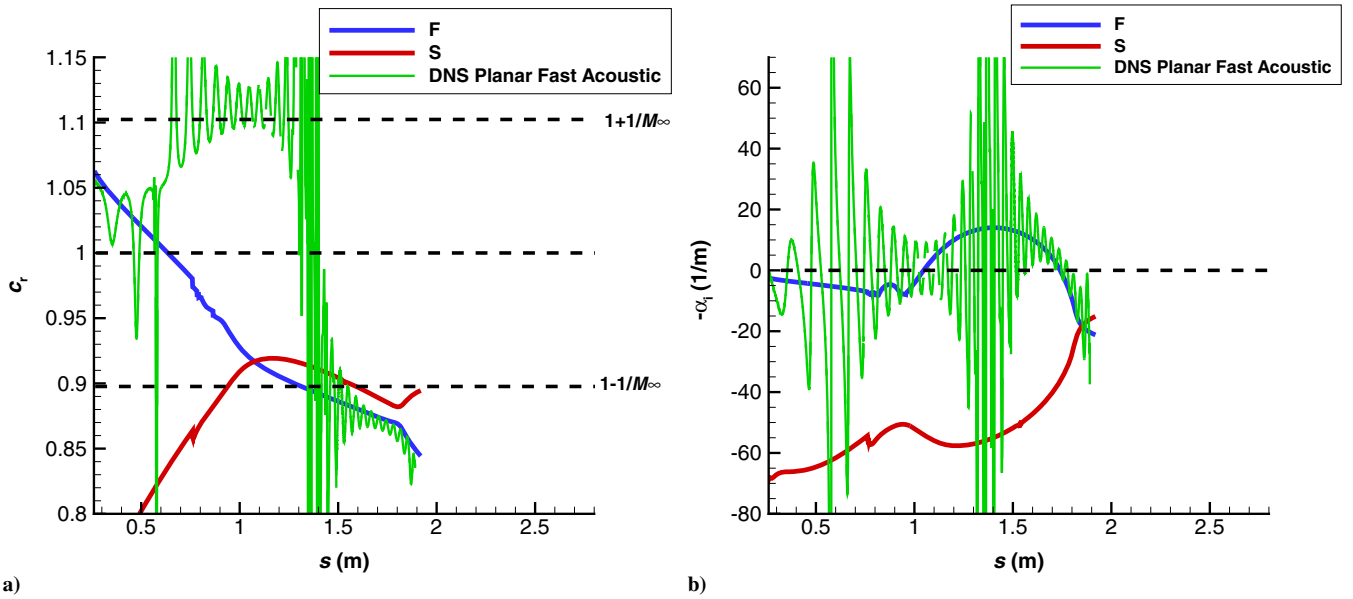

Fig. 21 Case B5 unsteady DNS results vs LST predicted results for 150 kHz disturbances: a) phase speed and b) growth rate.

become dominated by second mode instabilities until the far downstream regions of the cone. The growth rate shown in Fig. 21b is highly oscillatory and centered around a neutrally stable disturbance until approximately $s^* = 1.6$ m, whereas the phase speed plot in Fig. 21a shows similar oscillations centered around the continuous fast acoustic spectrum until the same point. These results indicate the dominance of neutrally stable forcing waves in the boundary layer. The observed amplification of the LST-predicted stable frequencies observed for case B5 in Fig. 20a can be attributed to the continuous introduction of weakly unstable/neutrally stable continuous mode forcing from the planar fast acoustic pulse.

Case B6 in Fig. 22 is shown to correlate much better with the 150 kHz LST results in terms of both phase speed and growth rate, though significant modal oscillations from the increased freestream forcing level are observed in the growth rate before approximately $s^* = 1.2$ m. From this it can be seen that case B6 behaves similarly to the finite spherical disturbances and primarily excites the second mode instability at this frequency. The results for case B7 and case B8 are strongly similar and are included in the Supplementary Figs. S6 and S7, respectively.

VII. Receptivity Results

The spectral receptivity coefficient for each of the disturbances was calculated using the methodology described in Sec. III.D. Using Huang and Zhong's method [9,22], the second mode receptivity coefficient is extracted through a combination of LST N-factors and unsteady DNS data. Isolating the contributions of individual modal disturbances allows for greater specificity when tracking the development of primary instabilities across a flow domain. More rigorous methods for decoupling the modal boundary-layer disturbances like the bi-orthogonal decomposition method developed by Tumin [43] and used by Miselis et al. [44] may be necessary to decompose more complex boundary-layer disturbance profiles and to characterize disturbance modes other than the second mode. However, this more rigorous decomposition model requires additional development before it can be applied to the results here.

A. Receptivity Coefficient Spectra

Because these receptivity calculations may be sensitive to sampling location [22], a comparison of the receptivity spectra for different sampling locations was made for the finite and planar pulse disturbances. The receptivity spectra for case B1 and case B2 at several sampling locations are presented in Fig. 23, whereas results for cases B3 and B4 are given in Supplementary Figs. S8 and S9, respectively. The chosen sampling locations were the LST branch I neutral stability point x_{brI}, the branch II neutral stability point x_{brII}, and an intermediate location defined at $x_{\mathrm{sample}} = 1.3 * x_{\mathrm{brI}}$, all of which are frequency dependent as seen in the neutral curve in Fig. 6. These points were chosen to ensure the sampling location remained within the unstable second mode region. After a sampling point is chosen for a given disturbance frequency, the normalized FFT decomposed surface pressure at that point is used as an input for Eq. (17). The branch I sampling point compares directly to conventional receptivity results like those reported by Balakumar and Chou [19], Kara et al. [20], Zhong and Ma [16], and Huang [22] as the normalization factor in this case is simply 1. Huang and Zhong stated that the boundary layer at the branch I neutral point is likely to be contaminated by the multimodal content of the disturbance, which may obscure the initial amplitudes of the primary instability modes of interest. In this study, cases B1–B4 in Fig. 23 demonstrate strong second mode dominance at all three sampling points. Although the branch I sampling case does show significantly more oscillations indicative of multimodal disturbances [22], the general shape and magnitude of the receptivity spectrum is in line with the other sampling locations.

It can be concluded that, for the finite spherical disturbances studied here so far, sampling location does not have a significant impact on the resulting receptivity coefficients, and that the second mode disturbance dominates the boundary-layer disturbances. This is likely because any extraneous forcing waves are primarily isolated to and damped out in the upstream regions of the cone and have little influence on the development of boundary-layer disturbances further downstream.

Figure 24 presents the same data for the planar fast and slow acoustic freestream pulses in case B5 and case B6, whereas the results for case B7 are given in the Supplementary Fig. S10 and the results of case B8 are given in Supplementary Fig. S11. The receptivity coefficient spectra for case B5 in Fig. 24a differ significantly from the finite spherical pulse cases, whereas the results in Fig. 24b for case B6 are similar to those in Fig. 23 for cases B1 and B2. The magnitudes of the receptivity coefficients for the planar cases are also much higher. This is because the additional forcing generated by the planar pulse as it propagates through the domain prevents the low-frequency disturbances from dampening significantly, as seen in Fig. 18. This results in significantly higher initial amplitudes for the second mode disturbances. The Fourier decomposition results presented in this study also do not account for the differences in wavenumber distributions between the finite spherical pulses and the infinite planar pulses.

Case B6 seems to very readily excite both second mode and additional low-frequency disturbances attributed to noise. The

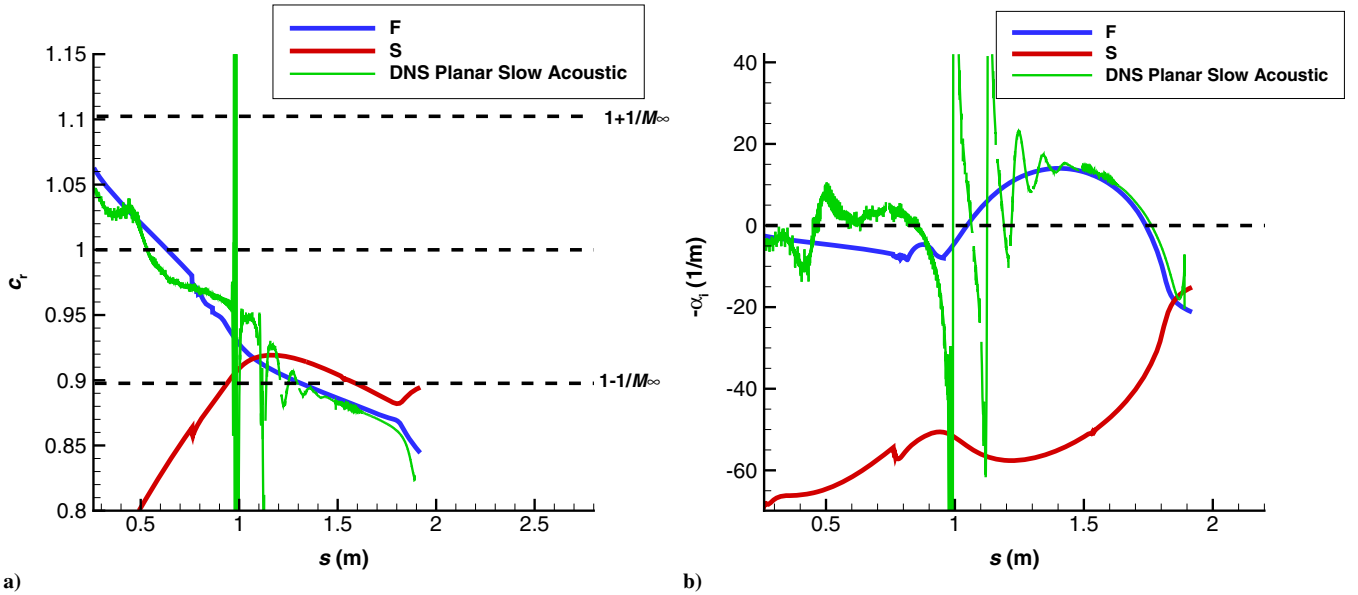

Fig. 22 Case B6 unsteady DNS results vs LST predicted results for 150 kHz disturbances: a) phase speed and b) growth rate.

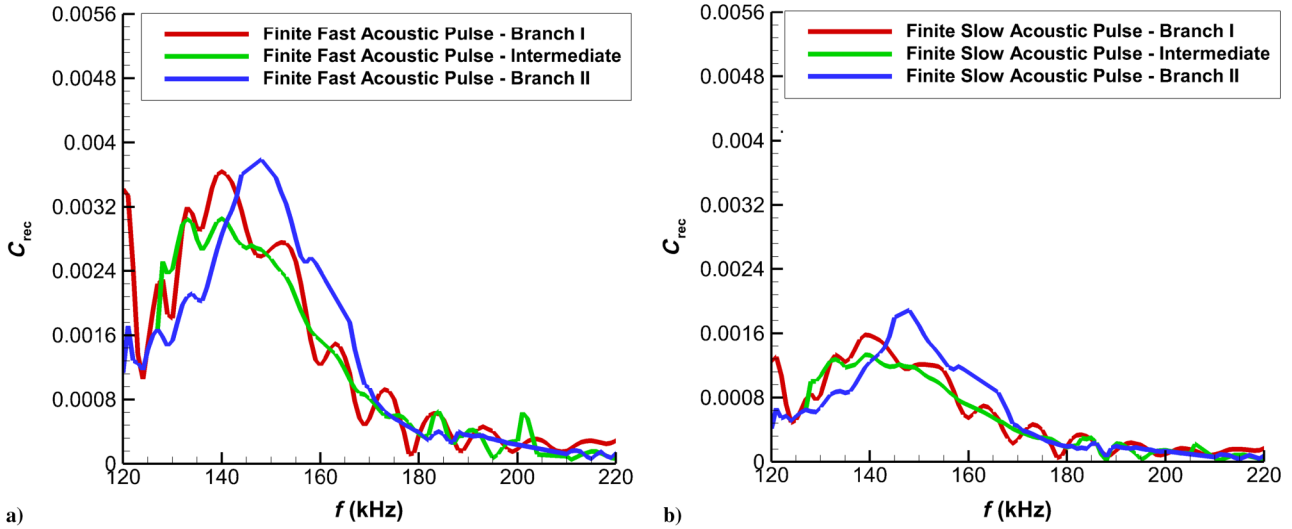

Fig. 23 Receptivity coefficients at different sampling locations for a) case B1 and b) case B2.

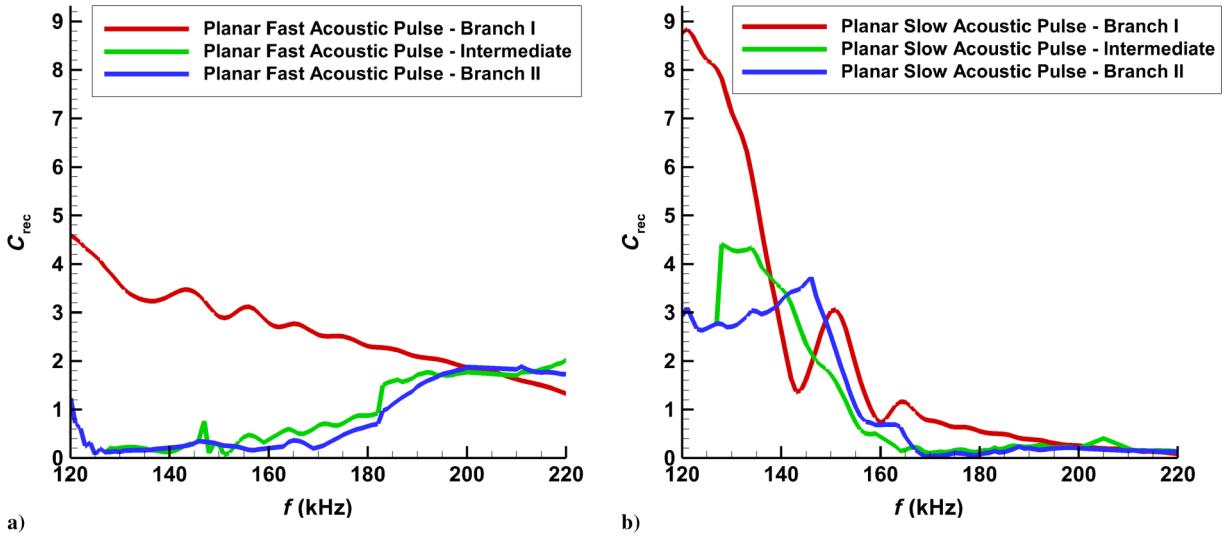

Fig. 24 Receptivity coefficients at different sampling locations for a) case B5 and b) case B6.

low-frequency disturbances in particular are observed to be excited much more strongly than in the finite pulse cases. This can also be seen in the FFT contours shown in Fig. 18, where again the low-frequency forcing generated by the planar pulse is observably much more present throughout the domain. The branch I sampling location results overpredicts the low-frequency response compared with the other sampling locations, indicating that modal decomposition is necessary to capture the behaviors of the second mode. On the other hand, the intermediate and branch II sampling locations show very similar results, peaking at frequencies between 125 and 145 kHz. A significant spike is seen in the intermediate sampling location near 138 kHz, whereas a similar spike is seen in the branch II sampling position near 145 kHz for case B6. These are attributed to nonparallel effects. Because of the relatively large nose bluntness of the cone, the boundary-layer variation upstream of $s^* = 1.0$ m may cause slight discrepancies between the LST and unsteady DNS results. This can be observed in the slight offset of the second mode amplification lobes and the branch II curves in Figs. 12 and 18. This is reflected in the difference in peak disturbance frequencies between the sampling points. Furthermore, the peak values vary somewhat between the two cases as well, with the intermediate sampling point having a peak coefficient approximately 9% higher than the branch II sampling case. Numerical resolution issues with the LST decomposition are assumed to play a role in this. However, these differences are relatively small and the overall disturbance development is still captured by the methodology here. A similar result is observed to a lesser degree in the finite pulse cases, but in general these nonparallel effects are weak and LST decomposition has been observed to effectively capture modal disturbance development here.

The receptivity spectra for case B5 in Fig. 24a differ significantly from cases B1, B2, and B6. The branch I sampling location produces a continuous broadband receptivity coefficient distribution, similar to the initial pulse. This indicates that the broadband forcing excited by the planar fast acoustic pulse is strong enough to mask the initial second mode instability at the branch I neutral point, and that the planar fast acoustic pulse excites a very broad range of frequencies in comparison to all the other cases. The combined disturbances at this location result in perturbation amplitudes far larger than those expected of the pure second mode. The other sampling locations also show that the receptivity coefficients are highest near 200 kHz, contrary to the finite spherical cases and LST results. Looking again at Fig. 18a it can be seen that an additional band of amplified disturbances can be found at these frequencies that is attributed to the strong surface forcing generated by the shock–disturbance interaction seen in Fig. 17. Although significant second mode amplification is observed in all of the cases, case B5 demonstrates that sufficiently noisy environments of fast acoustic disturbances can excite significant boundary-layer disturbances not associated with the second mode for this geometry. This can potentially account for the somewhat weak association between the

second mode and transition for this case that Marineau et al. observed [26].

The total receptivity spectra for the finite spherical cases (B1–B4) are shown in Fig. 25a and for the planar cases (B5–B8) in Fig. 25b at the intermediate sampling location. For the finite spherical pulses, it was found that the receptivity response was strongest for the fast acoustic, temperature, slow acoustic, and vorticity disturbances in that order. For the planar pulses the strongest second mode receptivity response was observed for the slow acoustic disturbance, followed by the temperature, vorticity, and fast acoustic pulses, though the planar fast acoustic pulse excited significant broadband waves in the boundary layer that were not associated with the second mode as well. These results can potentially be applied to improved transition prediction methods by providing the initial second mode receptivity response for a given freestream disturbance spectra. However, additional freestream disturbance configurations will be necessary before these results can be generalized sufficiently for broad application. These results can alternatively also be used in numerical studies investigating nonlinear breakdown phenomena, particularly in the reconstruction of controlled disturbance environments [21,45]. The spectral receptivity data can be used to isolate the response of a desired disturbance frequency and regenerate the dominant disturbance amplitude and phase as presented in the next section. This can be used as an inlet condition for nonlinear breakdown simulations, and greatly reduces the computational cost required to otherwise converge upstream mean flows and propagate desired disturbances downstream [21].

B. Disturbance Phase Angle Spectra

The phase angle spectra for the disturbance cases were also extracted from the unsteady DNS. With the data from the receptivity coefficient spectra and the phase angle spectra, the total initial receptivity response to an arbitrary axisymmetric freestream disturbance can be reconstructed [9,21]. These initial disturbances can then be used as inputs for more advanced transition predicted methods like Mack's amplitude method [27], Crouch's variable N-factor method [29], Marineau's iterative method [28], and Ustinov's implementation of the amplitude methods [46]. These data can also be used to reproduce arbitrary inlet conditions for downstream simulations studying phenomena such as nonlinear breakdown [21,45]. The receptivity phase angle spectra for the unsteady simulations are given in Fig. 26a for the finite spherical cases B1–B4, whereas Fig. 26b presents the same results for the planar disturbance cases B5–B8. These figures depict the FFT decomposed receptivity phase angles at the branch I neutral stability point for each disturbance frequency.

The profiles of the finite pulse cases in Fig. 26a and the planar cases in Fig. 26b are very similar, though the range of phase angles is smaller for the finite pulse cases. Because the disturbance pulse

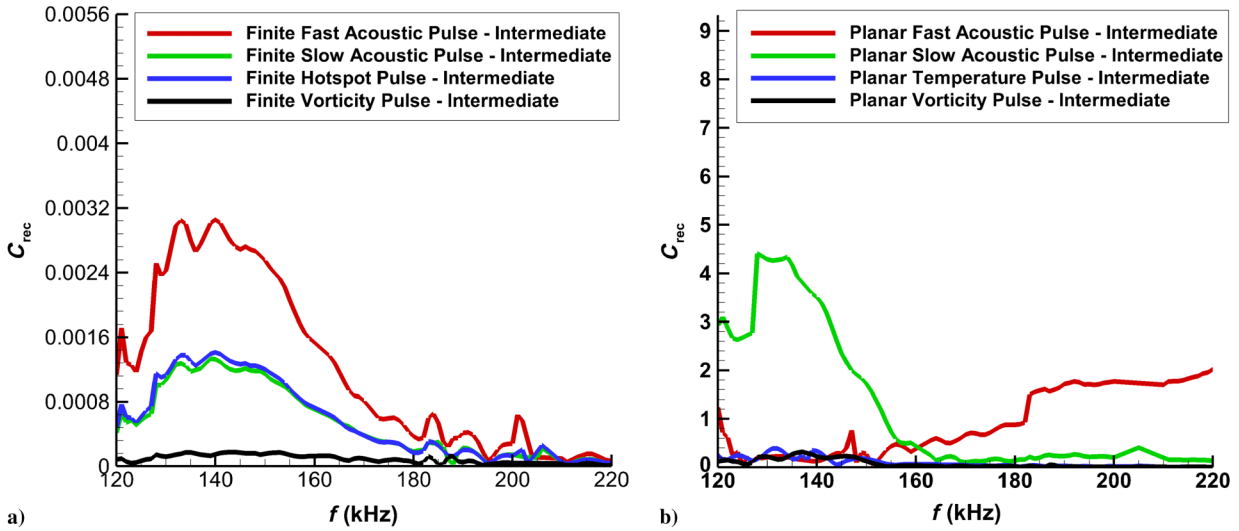

Fig. 25 Receptivity coefficient spectra for a) cases B1–B4 and b) cases B5–B8.

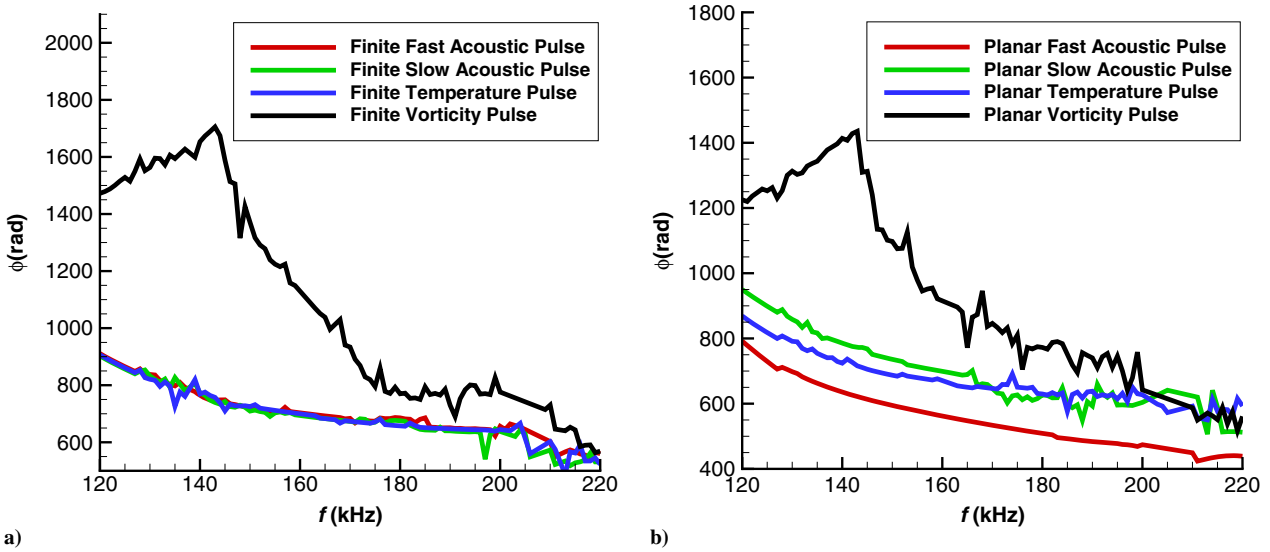

Fig. 26 Receptivity phase angle spectra for a) finite spherical disturbances (cases B1–B4) and b) planar disturbances (cases B5–B8) using the intermediate sampling position.

interacts with the mean flow only in the nose region of the cone, the finite pulse cases introduce much less forcing to the flow. This results in a much less noisy boundary-layer disturbance profile and a narrower band of phase angles for the finite pulse cases. On the other hand, the planar pulses continue to force the flow as they propagate downstream. Furthermore, as the different disturbance types propagate at different characteristic speeds in the freestream, an intrinsic phase difference is introduced between them. In both the finite and planar pulse cases, the phase angle spectra of the vorticity disturbances (cases B4 and B8) are observed to differ dramatically from the other disturbances at low frequencies near 120–140 kHz but begin to match better at higher frequencies near 200 kHz. This is likely to be due to the comparatively weak modal disturbance response that was observed for the vorticity disturbances, allowing for the flow to become more strongly influenced by low-frequency noise in the simulation.

VIII. Conclusions

The receptivity of a blunt cone at Mach 10 to a variety of freestream disturbances with broadband frequency spectra was investigated in this study. Spectral receptivity coefficient amplitudes and phase angles were extracted for finite spherical and planar geometry pulses consisting of fast acoustic, slow acoustic, temperature, and vorticity disturbances. The base flow geometry and freestream conditions were based on Marineau et al.'s experiments [26] and the numerical simulations were performed using a high-order shock fitting method (DNS). The stability of the mean flow was investigated using LST analysis and unsteady DNS. The pulses for unsteady DNS were modeled analytically in the freestream using Gaussian distributions to provide broadband frequency disturbances. The LST analysis showed that discrete mode F disturbances in a band of frequencies extending from approximately 118 to 238 kHz experienced second mode growth. An entropy layer was observed beginning near the nose and the frustum, which eventually merged into the boundary layer at $s^* = 0.9881$ m. Similar to Balakumar and Chou [19], LST and DNS did not predict peak second mode instability until after the entropy layer was swallowed. Good agreement was observed between the LST N-factor and Marineau et al.'s [26] PSE N-factor at the experimental transition location.

The unsteady DNS simulations were decomposed into their frequency components using FFT, which showed that all eight of the freestream pulse disturbances significantly excited the second mode on the cone. The finite spherical pulse cases (B1–B4) were observed to excite very similar boundary-layer disturbance profiles, with second mode disturbances beginning to dominate after $s^* = 1.2$ m. Because of their limited size, the finite pulses only interacted with the shock near the nose region of the cone. These isolated shock interactions allowed most of the initial broadband forcing to be damped out before second mode amplification began. The planar cases, which continued to perturb the flow as they propagated downstream, also demonstrated strong second mode amplification. The unsteady DNS results were validated against LST and showed good agreement for both the finite and planar pulse cases, though the planar fast acoustic pulse (case B5) demonstrated significantly stronger freestream forcing influences than the other unsteady cases. The strongest to weakest second mode response amplitudes for the finite pulses were observed for the fast acoustic (case B1), temperature (case B3), slow acoustic (case B2), and vorticity (case B4) pulses in that order. For the planar cases the slow acoustic pulse (case B6) generated the strongest second mode response followed by the temperature (case B7), vorticity (case B8), and finally fast acoustic (case B5) disturbances. Case B5 demonstrated weak second mode dominance relative to the other pulse cases, and instead indicated that the disturbance energy from the pulse is distributed to multiple instability modes in the boundary layer. This was not observed in the other cases and necessitates the use of more advanced modal decomposition methods, such as bi-orthogonal decomposition. Phase angle spectra were also extracted from the unsteady data and demonstrated strong agreement between the acoustic and entropy disturbances, though the vorticity pulses had significantly different phase spectra. This is attributed to the much weaker disturbance response to the vorticity pulses, potentially allowing for noise to pollute the phase spectra.

Using the receptivity and phase spectra found in this study, it is possible to reconstruct the receptivity response of the mean flow to arbitrary axisymmetric disturbances [9,21]. This can be directly used in the development and application of more advanced transition estimation procedures such as Crouch's [29] variable N-factor method or Mack's amplitude method [27] in order to improve the accuracy of transition predictions. However, additional steps need to be taken before the data provided here can be generalized to widespread application in the aforementioned amplitude methods. For one, non-axisymmetric disturbances must also be considered in order to further characterize the receptivity response of the studied mean flow to a wider range of potential experimental and flight conditions. This requires the simulation and study of three-dimensional broadband disturbances and the more complex disturbance environments that they may excite. Furthermore, additional comparisons to continuous freestream forcing similar to the study by Balakumar and Chou [19] as well as to experimental freestream response data would be necessary before more generalized receptivity correlations can be derived for direct use in the amplitude method. The application of more advanced multimode decomposition techniques may also be necessary to isolate disturbance modes of interest, as the methodology used here may not be able to isolate the second mode response in significantly noisy boundary layers.

Acknowledgments

This research was partially supported by the Air Force Office of Scientific Research (AFOSR) under AFOSR Grant #FA9550-19-10206 which was previously monitored by Dr. Ivett Leyva, and is presently monitored by Dr. Sarah H. Popkin. Additional support was provided by the Office of Naval Research (ONR) under Grant #N00014-17-2343, monitored by Dr. Eric Marineau. Primary computational resources were provided by Extreme Science and Engineering Discovery Environment (XSEDE) through the Texas Advanced Computing Center and the San Diego Supercomputer Center under grant number TG-ASC090076, supported in part by the National Science Foundation. Additional computational support was provided by the Department of Defense High Performance Computing Modernization Program through project AFOSR40702004. The views and conclusions contained herein are those of the authors and should not be interpreted as necessarily representing the official policies or endorsements, either expressed or implied, of the U.S. Air Force Office of Scientific Research, Office of Naval Research, XSEDE, or the U.S. Government.

References

[1] Fedorov, A., "Transition and Stability of High-Speed Boundary Layers," *Annual Review of Fluid Mechanics*, Vol. 43, No. 1, 2011, pp. 79–95. https://doi.org/10.1146/annurev-fluid-122109-160750

[2] Reshotko, E., "Hypersonic Stability and Transition," *Hypersonic Flows for Reentry Problems*, Vol. 1, No. A93-42576 17-02, 1991, pp. 18–34.

[3] Zhong, X., and Wang, X., "Direct Numerical Simulation on the Receptivity, Instability, and Transition of Hypersonic Boundary Layers," *Annual Review of Fluid Mechanics*, Vol. 44, No. 1, 2012, pp. 527–561. https://doi.org/10.1146/annurev-fluid-120710-101208

[4] Ma, Y., and Zhong, X., "Receptivity of a Supersonic Boundary Layer over a Flat Plate. Part 3. Effects of Different Types of Free-Stream Disturbances," *Journal of Fluid Mechanics*, Vol. 532, June 2005, pp. 63–109. https://doi.org/10.1017/S0022112005003836

[5] Mack, L. M., "Boundary Layer Stability Theory," Jet Propulsion Lab. TR 900-277, Pasadena, CA, 1969.

[6] Schneider, S., "Effects of High-Speed Tunnel Noise on Laminar-Turbulent Transition," *Journal of Spacecraft and Rockets*, Vol. 38, No. 3, 2001, pp. 323–333. https://doi.org/10.2514/2.3705

[7] Kovasznay, L. S. G., "Turbulence in Supersonic Flow," *Journal of the Aeronautical Sciences*, Vol. 20, No. 10, 1953, pp. 657–682. https://doi.org/10.2514/8.2793

[8] McKenzie, J. F., and Westphal, K. O., "Interaction of Linear Waves with Oblique Shock Waves," *Physics of Fluids*, Vol. 11, No. 11, 1968, pp. 2350–2362. https://doi.org/10.1063/1.1691825

[9] Huang, Y., and Zhong, X., "Numerical Study of Hypersonic Boundary-Layer Receptivity and Stability with Freestream Hotspot Perturbations," *AIAA Journal*, Vol. 52, No. 12, 2014, pp. 2652–2672. https://doi.org/10.2514/1.J052657

[10] Balakumar, P., and Malik, M., "Discrete Modes and Continuous Spectra in Supersonic Boundary Layers," *Journal of Fluid Mechanics*, Vol. 239, June 1992, pp. 631–656. https://doi.org/10.1017/S0022112092004555

[11] Ma, Y., and Zhong, X., "Receptivity of a Supersonic Boundary Layer over a Flat Plate. Part 1. Wave Structures and Interactions," *Journal of Fluid Mechanics*, Vol. 488, July 2003, pp. 31–78. https://doi.org/10.1017/S0022112003004786

[12] Ma, Y., and Zhong, X., "Receptivity of a Supersonic Boundary Layer over a Flat Plate. Part 2. Receptivity to Freestream Sound," *Journal of Fluid Mechanics*, Vol. 488, July 2003, pp. 79–121. https://doi.org/10.1017/S0022112003004798

[13] Malik, M., and Balakumar, P., "Receptivity of Supersonic Boundary Layers to Acoustic Disturbances," *35th AIAA Fluid Dynamics Conference and Exhibit*, AIAA Paper 2005-5027, 2005. https://doi.org/10.2514/6.2005-5027

[14] Fedorov, A. V., "Receptivity of a High-Speed Boundary Layer to Acoustic Disturbances," *Journal of Fluid Mechanics*, Vol. 491, Sept. 2003, pp. 101–129. https://doi.org/10.1017/S0022112003005263

[15] Fedorov, A. V., Ryzhov, A. A., Soudakov, V. G., and Utyuzhnikov, S. V., "Receptivity of a High-Speed Boundary Layer to Temperature Spottiness," *Journal of Fluid Mechanics*, Vol. 722, May 2013, pp. 533–553. https://doi.org/10.1017/jfm.2013.111

[16] Zhong, X., and Ma, Y., "Boundary-Layer Receptivity of Mach 7.99 Flow over a Blunt Cone to Free-Stream Acoustic Waves," *Journal of Fluid Mechanics*, Vol. 556, June 2006, pp. 55–103. https://doi.org/10.1017/S0022112006009293

[17] Balakumar, P., and Kegerise, M., "Receptivity of Hypersonic Boundary Layers over Straight and Flared Cones," *48th AIAA Aerospace Sciences Meeting Including the New Horizons Forum and Aerospace Exposition*, AIAA Paper 2010-1065, 2010. https://doi.org/10.2514/6.2010-1065

[18] Balakumar, P., and Kegerise, M., "Receptivity of Hypersonic Boundary Layers to Acoustic and Vortical Disturbances," *49th AIAA Aerospace Sciences Meeting Including the New Horizons Forum and Aerospace Exposition*, AIAA Paper 2011-0371, 2011. https://doi.org/10.2514/6.2011-371

[19] Balakumar, P., and Chou, A., "Transition Prediction in Hypersonic Boundary Layers Using Receptivity and Freestream Spectra," *AIAA Journal*, Vol. 56, No. 1, 2018, pp. 2593–2606. https://doi.org/10.2514/1.J056040

[20] Kara, K., Balakumar, P., and Kandil, O., "Effects of Nose Bluntness on Hypersonic Boundary-Layer Receptivity and Stability over Cones," *AIAA Journal*, Vol. 55, No. 12, 2011, pp. 2593–2606. https://doi.org/10.2514/1.J050032

[21] Lei, J., and Zhong, X., "Numerical Simulation of Freestream Waves Receptivity and Breakdown in Mach 6 Flow over Cone," *43rd Fluid Dynamics Conference*, AIAA Paper 2013-2741, 2013. https://doi.org/10.2514/6.2013-2741

[22] Huang, Y., "Numerical Study of Hypersonic Boundary-Layer Receptivity and Stability with Freestream Hotspot Perturbations," Ph.D. Thesis, Univ. of California, Los Angeles, CA, 2016.

[23] Wheaton, B., Juliano, T., Berridge, D., Chou, A., Gilbert, P., Casper, K., Steen, L., and Schneider, S., "Instability and Transition Measurements in the Mach-6 Quiet Tunnel," *39th AIAA Fluid Dynamics Conference*, AIAA Paper 2009-3559, 2009. https://doi.org/10.2514/6.2009-3559

[24] Chou, A., "Characterization of Laser-Generated Perturbations and Instability Measurements on a Flared Cone," Master's Thesis, Purdue Univ., West Lafayette, IN, 2010.

[25] Chou, A., Wheaton, B., Ward, C., Gilbert, P., Steen, L., and Schneider, S., "Instability and Transition Reserach in a Mach-6 Quiet Tunnel," *49th AIAA Aerospace Sciences Meeting*, AIAA Paper 2011-0283, 2011. https://doi.org/10.2514/6.2011-283

[26] Marineau, E., Moraru, C., Lewis, D., Norris, J., and Lafferty, J., "Mach 10 Boundary-Layer Transition Experiments on Sharp and Blunted Cones," *19th AIAA International Space Planes and Hypersonic Systems and Technologies Conference*, AIAA Paper 2014-3108, 2014. https://doi.org/10.2514/6.2014-3108

[27] Mack, L. M., "Transition Prediction and Linear Stability Theory," Jet Propulsion Lab. TR AGARD CP-224, Pasadena, CA, 1977.

[28] Marineau, E., "Prediction Methodology for Second-Mode Dominated Boundary-Layer Transition in Wind Tunnels," *AIAA Journal*, Vol. 55, No. 2, 2017, pp. 484–499. https://doi.org/10.2514/1.J055061

[29] Crouch, J., and Ng, L., "Variable N-Factor Method for Transition Prediction in Three-Dimensional Boundary Layers," *AIAA Journal*, Vol. 38, No. 2, 2000, pp. 211–216. https://doi.org/10.2514/2.973

[30] Williamson, J., "Low-Storage Runge-Kutta Schemes," *Journal of Computational Physics*, Vol. 35, No. 1, 1980, pp. 48–56. https://doi.org/10.1016/0021-9991(80)90033-9

[31] Zhong, X., "High-Order Finite-Difference Schemes for Numerical Simulation of Hypersonic Boundary-Layer Transition," *Journal of Computational Physics*, Vol. 144, No. 2, 1998, pp. 662–709. https://doi.org/10.1006/jcph.1998.6010

[32] Malik, M. R., "Numerical Methods for Hypersonic Boundary Layer Stability," *Journal of Computational Physics*, Vol. 86, No. 2, Feb. 1990, pp. 376–413. https://doi.org/10.1016/0021-9991(90)90106-B

[33] Lei, J., and Zhong, X., "Linear Stability Analysis of Nose Bluntness Effects on Hypersonic Boundary Layer Transition," *Journal of Spacecraft and Rockets*, Vol. 49, No. 1, 2012, pp. 24–37. https://doi.org/10.2514/1.52616

[34] Aleksandrova, E., Novikov, A., Utyuzhnikov, S., and Fedorov, A., "Experimental Study of the Laminar-Turbulent Transition on a Blunt Cone," *Journal of Applied Mechanics and Technical Physics*, Vol. 55, No. 3, 2014, pp. 375–385. https://doi.org/10.1134/S0021894414030018

[35] Zhong, X., "Leading-Edge Receptivity to Free Stream Disturbance Wave for Hypersonic Flow over a Parabola," *Journal of Fluid Mechanics*, Vol. 441, Aug. 2001, pp. 315–367. https://doi.org/10.1017/S0022112001004918

[36] Lei, J., and Zhong, X., "Linear Stability Analysis of Nose Bluntness Effects on Hypersonic Boundary Layer Transition," *48th AIAA Aerospace Sciences Meeting Including the New Horizons Forum and Aerospace Exposition*, AIAA Paper 2010-0898, 2010. https://doi.org/10.2514/6.2010-898

[37] He, S., and Zhong, X., "Numerical Study of Hypersonic Boundary Layer Receptivity over a Blunt Cone to Freestream Pulse Disturbances," *AIAA Aviation 2020 Forum*, AIAA Paper 2020-2996, 2020. https://doi.org/10.2514/6.2020-2996

[38] Knisely, C. P., and Zhong, X., "Significant Supersonic Modes and the Wall Temperature Effect in Hypersonic Boundary Layers," *AIAA Journal*, Vol. 57, No. 4, 2019, pp. 1552–1566. https://doi.org/10.2514/1.J057775

[39] Knisely, C. P., and Zhong, X., "Sound Radiation by Supersonic Unstable Modes in Hypersonic Blunt Cone Boundary Layers. I. Linear Stability Theory," *Physics of Fluids*, Vol. 31, No. 2, 2019, Paper 024103. https://doi.org/10.1063/1.5055761

[40] Knisely, C. P., and Zhong, X., "Sound Radiation by Supersonic Unstable Modes in Hypersonic Blunt Cone Boundary Layers. II. Direct Numerical Simulation," *Physics of Fluids*, Vol. 31, No. 2, 2019, Paper 024104. https://doi.org/10.1063/1.5077007

[41] Mortensen, C. H., "Toward an Understanding of Supersonic Modes in Boundary-Layer Transition for Hypersonic Flow over Blunt Cones," *Journal of Fluid Mechanics*, Vol. 846, July 2018, pp. 789–814. https://doi.org/10.1017/jfm.2018.246

[42] Mack, L. M., "Boundary Layer Linear Stability Theory," Advisory Group for Aerospace Research and Development TR 709, Neuilly-sur-Seine, France, 1984.

[43] Tumin, A., "Three-Dimensional Spatial Normal Modes in Compressible Boundary Layers," *Journal of Fluid Mechanics*, Vol. 586, Sept. 2007, pp. 295–322. https://doi.org/10.1017/S002211200700691X

[44] Miselis, M., Huang, Y., and Zhong, X., "Modal Analysis of Receptivity Mechanisms for a Freestream Hot-Spot Perturbation on a Blunt Compression-Cone Boundary Layer," *46th AIAA Fluid Dynamics Conference*, AIAA Paper 2016-3345, 2016. https://doi.org/10.2514/6.2016-3345

[45] Sivasubramanian, J., and Fasel, H. F., "Direct Numerical Simulation of Transition in a Sharp Cone Boundary Layer at Mach 6: Fundamental Breakdown," *Journal of Fluid Mechanics*, Vol. 768, April 2015, pp. 175–218. https://doi.org/10.1017/jfm.2014.678

[46] Ustinov, M. V., "Amplitude Method of Prediction of Laminar-Turbulent Transition on a Swept-Wing," *Fluid Dynamics*, Vol. 52, No. 1, 2017, pp. 71–87. https://doi.org/10.1134/S0015462817010070

C. Wen
Associate Editor